

# The T2K Fine-Grained Detectors

P.-A. Amaudruz<sup>a</sup>, M. Barbi<sup>d</sup>, D. Bishop<sup>a</sup>, N. Braam<sup>g</sup>, D.G. Brook-Roberge<sup>b</sup>, S. Giffin<sup>d</sup>, S. Gomi<sup>f</sup>, P. Gumplinger<sup>a</sup>, K. Hamano<sup>a</sup>, N.C. Hastings<sup>d</sup>, S. Hastings<sup>b</sup>, R.L. Helmer<sup>a,\*</sup>, R. Henderson<sup>a</sup>, K. Ieki<sup>f</sup>, B. Jamieson<sup>b</sup>, I. Kato<sup>a</sup>, N. Khan<sup>a</sup>, J. Kim<sup>b</sup>, B. Kirby<sup>b</sup>, P. Kitching<sup>c</sup>, A. Konaka<sup>a</sup>, M. Lenckowski<sup>g,a</sup>, C. Licciardi<sup>d</sup>, T. Lindner<sup>b</sup>, K. Mahn<sup>a</sup>, E.L. Mathie<sup>d</sup>, C. Metelko<sup>h</sup>, C.A. Miller<sup>a</sup>, A. Minamino<sup>f</sup>, K. Mizouchi<sup>a</sup>, T. Nakaya<sup>f</sup>, K. Nitta<sup>f</sup>, C. Ohlmann<sup>a</sup>, K. Olchanski<sup>a</sup>, S.M. Oser<sup>b</sup>, M. Otani<sup>f</sup>, P. Poffenberger<sup>g</sup>, R. Poutissou<sup>a</sup>, J.-M. Poutissou<sup>a</sup>, W. Qian<sup>h</sup>, F. Retiere<sup>a</sup>, R. Tacik<sup>d</sup>, H.A. Tanaka<sup>b</sup>, P. Vincent<sup>a</sup>, M. Wilking<sup>a</sup>, S. Yen<sup>a</sup>, M. Yokoyama<sup>e</sup>

<sup>a</sup>*TRIUMF, Vancouver, British Columbia, Canada*

<sup>b</sup>*University of British Columbia, Department of Physics and Astronomy, Vancouver, British Columbia, Canada*

<sup>c</sup>*University of Alberta, Centre for Particle Physics, Department of Physics, Edmonton, Alberta, Canada*

<sup>d</sup>*University of Regina, Physics Department, Regina, Saskatchewan, Canada*

<sup>e</sup>*University of Tokyo, Department of Physics, Tokyo, Japan*

<sup>f</sup>*Kyoto University, Department of Physics, Kyoto, Japan*

<sup>g</sup>*University of Victoria, Department of Physics and Astronomy, Victoria, British Columbia, Canada*

<sup>h</sup>*STFC, Rutherford Appleton Laboratory, Harwell Oxford, United Kingdom*

---

## Abstract

T2K is a long-baseline neutrino oscillation experiment searching for  $\nu_e$  appearance in a  $\nu_\mu$  beam. The beam is produced at the J-PARC accelerator complex in Tokai, Japan, and the neutrinos are detected by the Super-Kamiokande detector located 295 km away in Kamioka. A suite of near detectors (ND280) located 280 m downstream of the production target is used to characterize the components of the beam before they have had a chance to oscillate and to better understand various neutrino interactions on several nuclei. This paper describes the design and construction of two massive fine-grained detectors (FGDs) that serve as active targets in the ND280 tracker. One FGD is composed solely of scintillator bars while the other is partly scintillator and partly water. Each element of the FGDs is described, including the wavelength shifting fiber and Multi-Pixel Photon Counter used to collect the light signals, the readout electronics, and the calibration system. Initial tests and *in situ* results of the FGDs' performance are also presented.

---

## 1. Introduction

The Tokai-to-Kamioka (T2K) experiment [1] is studying neutrino oscillations using a man-made neutrino beam sent from the Japan Proton Accelerator Research Complex (J-PARC) in Tokai, Japan, towards the Super-Kamiokande detector [2], located 295 km away. T2K is the first experiment to make use of an off-axis configuration [3, 4, 5], which provides a relatively narrow band beam, in this case peaked around 700 MeV.

A magnetized near detector called ND280, situated 280 m downstream from the hadron production target in J-PARC, measures the neutrino beam's properties before the neutrinos have had a chance to oscillate. It can therefore be used to predict the neutrino event rate and energy spectrum at Super-Kamiokande in the absence of oscillations. As well, interaction rates or cross sections for several neutrino reaction channels in the 100 MeV to few GeV energy range will be measured.

ND280 contains several subdetectors optimized to measure neutrino interactions in this energy range [6]. This paper describes the design

---

\*Corresponding author

*Email address:* helmer@triumf.ca (R.L. Helmer)

and performance of ND280's two massive Fine-Grained Detectors (FGDs), which provide target mass for neutrino interactions as well as tracking of charged particles emerging from the interaction vertex. The FGDs form part of ND280's tracker. The tracker, consisting of three large time projection chambers (TPCs) [7] and the two FGD modules, lies at the heart of ND280 (see Fig. 1). The primary function of ND280 is to measure the neutrino beam's flux, energy spectrum, and flavor composition by observing charged current neutrino interactions. The FGDs are thin enough ( $\sim 30$  cm) that most of the penetrating particles produced in neutrino interactions, especially muons, reach the TPCs where their momenta and charges are measured by their curvature in the  $\sim 0.2$  T magnetic field. While the TPCs provide excellent 3D tracking and particle identification for forward- and backward-going charged particles, short-ranged particles such as recoil protons are primarily measured in the FGDs themselves. The FGDs therefore have fine granularity so that individual particle tracks can be resolved and their directions measured.

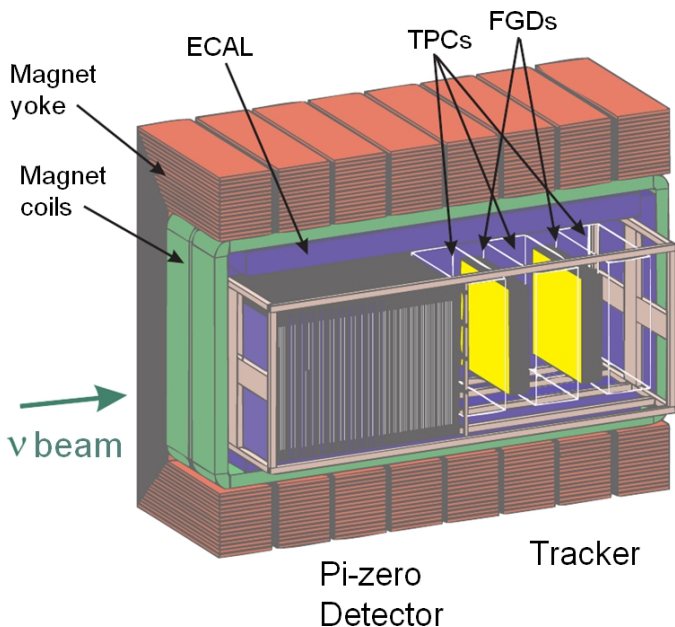


Figure 1: Cutaway view of the ND280 detector. The two FGDs are located between three TPCs. A Pi-Zero Detector sits upstream of the tracker region, and electromagnetic calorimeters (ECAL) surrounds all of the central detectors. The magnetic field is in the horizontal direction perpendicular to the beam.

An especially important reaction to measure is the CCQE interaction  $\nu_\ell + n \rightarrow \ell^- + p$ , which is the most common interaction at T2K's beam energy. For these interactions, the energy of the incident neutrino is calculable from only the energy and direction of the final lepton, with an accuracy limited by the Fermi momentum of the neutron in the nucleus. The CCQE interaction cross section is relatively simple to model theoretically [8], and is well constrained by data [9, 10, 11]. CCQE interactions therefore provide an ideal means of measuring the neutrino beam's energy spectrum and flux in the near detector, which can then be used to predict the event rate and energy spectrum at the far detector.

Although the CCQE interaction is the most common interaction mode, many other processes occur. An important example is CC single pion (CC-1 $\pi$ ) production ( $\nu_\ell + N \rightarrow \ell^- + N' + \pi$ ). This process often proceeds through excitation of a  $\Delta$  resonance and is indistinguishable from a CCQE event in Super-K, where only the final state charged lepton is above the Cherenkov threshold. Because CC-1 $\pi$  produces a three-body final state, the initial neutrino's energy is not a simple function of the charged lepton's direction and energy. CC-1 $\pi$  events will therefore smear out the energy spectrum measurement, and every effort is made to exclude them from the energy spectrum analyses in both the near and far detectors. At Super-K this is accomplished by selecting only events with a single charged lepton in the final state, although CC-1 $\pi$  events with the pion below Cherenkov threshold form an irreducible background. The ND280 tracker is used to measure the size of this and other backgrounds to CCQE interactions at Super-K.

The rates of these CCQE and non-QE interactions from the T2K beam must be well determined in the tracker so that a satisfactory prediction can be made of the unoscillated event rates at Super-K. Because the tracker can see all charged particles produced in an interaction, it can identify CCQE events by selecting just those events which contain a lepton and a recoil proton. Events containing pions can be rejected by searching for additional charged tracks near the vertex, identify-

ing Michel electrons produced by pions stopping in an FGD through the  $\pi \rightarrow \mu \rightarrow e$  decay chain, or by testing the consistency of a track’s deposited charge, direction, and momentum with the CCQE hypothesis.

The FGDs must therefore satisfy a variety of design criteria:

- They must be capable of detecting all charged particles produced at the interaction vertex with good efficiency in order to determine the type of interaction.
- They must be thin enough that charged leptons will penetrate into the TPCs where their momenta and flavor can be determined.
- The directions of recoil protons must be measured so that CCQE events can be selected using kinematic constraints on the recoil proton’s direction.
- Particle ID from  $dE/dx$  measurements must distinguish protons from muons and pions.
- The tracker must contain  $\sim 1$  tonne of target mass for neutrino interactions in order to yield a sufficient statistical sample of events.
- Because the ND280 sits in an off-axis beam, the off-axis angle and hence the neutrino energy spectrum varies substantially across the face of the tracker. Nonuniformities in threshold or efficiency across the tracker would greatly complicate the extraction of the neutrino beam properties and could potentially bias the measurement. Therefore the detector response across the tracker needs to be as uniform as practically possible.
- Because the far detector is a water Cherenkov detector, the tracker must measure the neutrino interaction rates on water. All of the relevant neutrino cross sections depend at some level on the target nucleus through such effects as Pauli blocking, pion rescattering and absorption inside the nucleus, etc. These nuclear effects cannot be reliably corrected for from theory, and therefore the nuclear interaction rates must be measured on water

so that the rates can be used to predict the rates for these processes in Super-K.

- The FGD electronics must provide for acceptance of late hits such as those due to Michel electrons.

### 1.1. Overview of the FGD design

The functional unit of an FGD is a single extruded polystyrene scintillator bar (described in Section 2) oriented perpendicular to the beam in either the  $x$  or  $y$  direction. To achieve the necessary fine granularity, the bars have a square cross section 9.6 mm on a side. They are arranged into modules, each “XY module” consisting of a layer of 192 scintillator bars in the horizontal direction glued to 192 bars in the vertical direction (see Section 3). FGD1 contains fifteen such modules while FGD2 contains seven. Each module has dimensions of  $186.4 \times 186.4 \times 2.02$  cm (not including electronics). Each scintillator bar has a reflective coating containing  $\text{TiO}_2$  and a wavelength shifting (WLS) fiber (Section 4) going down an axial hole. An air gap provides the coupling between the scintillator and fiber. The fiber extends a few centimeters from one end of the bar to reach a Multi-Pixel Photon Counter (MPPC) [12, 13] (see Section 5), which senses and digitizes the light signals. Within an  $x$  or  $y$  layer alternating fibers are read out from alternating ends. To improve light collection efficiency, the exposed ends of the fibers are mirrored by vacuum deposition of aluminum. An LED-based light injection system that flashes the exposed ends permits *in situ* calibration of photosensor response, saturation, and nonlinearity (see Section 8.7). The photosensors are mounted along all four sides of the XY module on busboards screwed directly into the edges of the module.

In addition to seven XY modules, FGD2 also contains six water target modules (described in Section 6). These are sheets of thin-walled hollow corrugated polycarbonate, 2.5 cm thick, whose ends have been sealed with polyurethane sealant. The modules are filled with water to provide a layer of water target. The water is maintained under subatmospheric pressure by a vacuum pump

system so that if a leak develops the system will suck air into the modules rather than spilling water inside the FGD. Comparing the interaction rates in the two FGDs permits separate determination of cross sections on carbon and water.

Each FGD has outer dimensions of 230 cm (width)  $\times$  240 cm (height)  $\times$  36.5 cm (depth in beam direction), and contains 1.1 tonnes of target material. They were built with the same geometry, mounting, and readout for interoperability.

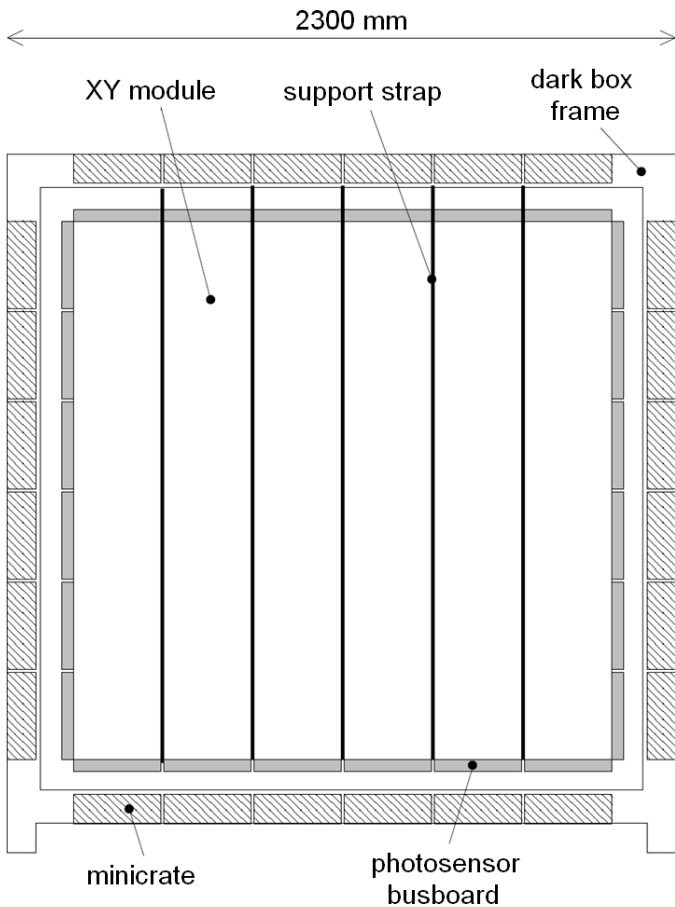


Figure 2: Cross-sectional view of an FGD, showing the locations of the scintillator modules, photosensors, support straps, electronics minicrates, and dark box.

The XY modules and target water modules hang inside a lighttight box called a “dark box”. Each module is supported by five stainless steel straps that loop around the bottom of the module and attach to anchor points in the top side of the dark box. The dark box itself is a sturdy aluminum frame that supports the weight of the FGD modules and transfers that weight to the detector basket. The walls of the dark box are

made of thin opaque panels to keep its interior lighttight. Further details can be found in Section 7.

The FGD’s front-end electronics resides in 24 minicrates that attach to the outside of the four sides of the dark box. Signals from the photosensors inside the dark box are carried from the photosensor busboards to the electronics by ribbon cables that attach to the crates’ backplanes, which are mounted over apertures on the four sides of the box. The minicrates are cooled by a subatmospheric pressure water cooling system running along the sides of the frame of the dark box, and power is carried to the minicrates by a power bus mounted on the frame. The electronics is arranged so that all heat-producing elements are located outside the dark box in the minicrates where they can be readily cooled by the cooling system, while only elements with negligible power dissipation (the photosensors themselves) are present inside the dark box itself. The electronics modules in the minicrates control the operation of the photosensors and process the signals from them; details are presented in Section 8.

A cross-sectional view of an FGD, as viewed by the beam, is given in Fig. 2, showing the location of the XY modules, photosensor busboards, dark box, and minicrates.

Digitized data from each minicrate are read out over optical fiber links to Data Collector Cards (DCCs) located outside the magnet. The DCCs compress the data and pass it to the DAQ system (described in Section 9). Slow control systems (Section 10) use a separate data and power bus for redundancy.

This paper will review the design, construction, and testing of each FGD component, briefly described in the foregoing, and will present results on the detector performance from calibration efforts (Section 11), beam tests (Section 12), and neutrino data-taking periods (Section 13).

## 2. Scintillator bars

Fabrication of the scintillator bars and associated quality control measurements are discussed in this section.

### 2.1. Geometrical specification

The geometrical design specifications of each bar are as follows:

- Length =  $1864.3 \pm 0.3$  mm
- Overall width and height =  $9.61 \pm 0.2$  mm
- TiO<sub>2</sub> thickness =  $0.25 \pm 0.05$  mm, (co-extruded bar coating)
- Active dimensions =  $9.1 \pm 0.2$  mm
- Hole diameter =  $1.8 \pm 0.3$  mm

The total number of bars produced, including  $\sim 3500$  spares, was 11900.

Section 3 describes how the scintillator bars are assembled into XY modules.

### 2.2. Materials specification

The scintillator bars were made of polystyrene doped with PPO and POPOP, and were co-extruded with a reflective coating consisting of polystyrene doped with TiO<sub>2</sub>. The materials used in extruding the bars were as follows. For the basic polystyrene, DOW Styron 663 W-27 general purpose crystal polystyrene in pellet form, without additives, was used. The fluors were purchased already mixed from Curtiss Laboratories ([curtisslabs.lookchem.com](http://curtisslabs.lookchem.com)). The primary fluor was 1 % PPO (2,5-diphenyloxazole) and the secondary fluor was 0.03 % POPOP (1,4-bis(5-phenyloxazol-2-yl) benzene). The TiO<sub>2</sub> concentrate was purchased from Clariant (catalog number WHC-26311-A). This concentrate has 60 % TiO<sub>2</sub> (rutile form). With 1 part concentrate to 3 parts plain polystyrene pellets by weight, the concentration of TiO<sub>2</sub> in the coating was 15 %.

### 2.3. Mixing and extrusion procedures

Preparations for fabricating the bars were carried out at TRIUMF. The polystyrene pellets were weighed in 100 lb batches and dried for  $\sim 8$  hours at 170 °F with dry N<sub>2</sub> flowing in the oven. The pellets were then mixed in a small concrete mixer, which had dry N<sub>2</sub> from a liquid N<sub>2</sub> dewar flowing through it, with the pre-mixed PPO/POPOP fluor. This mixture was

then stored in 200 lb containers under dry N<sub>2</sub> purge. The TiO<sub>2</sub> coating (15 lb polystyrene to 5 lb TiO<sub>2</sub> concentrate) was mixed by hand and similarly dried and stored. The materials, mixing and extrusion procedures were identical to those utilized in producing extruded scintillator bars for MINOS [14] and K2K SciBar [15].

The mixed materials were transported to Celco Plastics Ltd, Surrey, B.C., where they were purged with dry N<sub>2</sub>, then fed into hoppers. Separate hoppers were used for the doped plastic scintillator extrusion and for the TiO<sub>2</sub> co-extrusion. The materials were heated to a molten state and forced through the die and sizer plate, which determine the bar cross section. The hole in the center of the bar was formed by passing an air stream through a nozzle in the center of the die. The bar was then cooled by pulling it through a water bath and cut to length by an automated saw which moved with the bar. A laser feedback system controlled the bar thickness.

During the production run steps were taken to insure the bars met the following specifications.

- Each bar was labeled with a bar code (bar code and number) just after it was cut by the saw.
- Burrs were removed from the holes and the edges of the bar using a utility knife.
- A stainless steel rod was threaded through the bar's hole to check for blockages.
- The bar was fed into a jig containing dial gauges to measure the widths in the  $x$  and  $y$  directions.
- The bar code was scanned and then a computer automatically read out the  $x$  and  $y$  widths of the bar. This information was stored with a time stamp.
- If the bar was out of tolerance ( $9.6 \pm 0.1$  mm) the attention of a Celco operator was raised to investigate the change.
- Every 1-2 hours a small ( $\sim 5$  cm) piece of scintillator was cut and polished using successively finer graded sandpaper. The piece

was placed into a holding jig so that a photo of the polished end could be taken. Software to find the  $\text{TiO}_2$  boundaries and hole boundaries was used to measure the critical dimensions. Fig. 3 shows a photo of the bar profile with the measured dimensions for a typical bar.

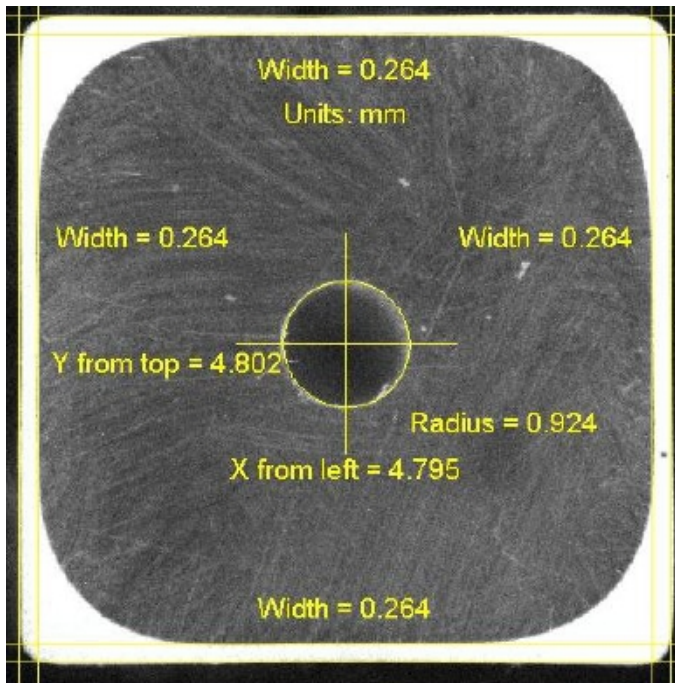


Figure 3: Photo taken with a CCD camera of a typical scintillator bar produced at Celco Plastics. A MATLAB<sup>®</sup> edge-finding routine is used to find the edges of the  $\text{TiO}_2$  to measure the  $\text{TiO}_2$  thickness on all 4 sides, and the edge of the center hole to measure the hole diameter.

- After every shift the bars produced during the shift were taken back to TRIUMF and 4-8 bars out of every 100 were scanned on the bar scanner (see section 2.5) to make sure the light yield was acceptable.

#### 2.4. Bar width results

This section summarizes the results of the dial gauge measurements on the bars as they came off the production run. There were four dial gauges in total: two to measure the width of the bar and two to measure the height. The resolution of the dial gauges was 0.01 mm. The distributions are shown in Fig. 4. The RMS of the deviations ranges from 0.013 mm for the height to 0.019 mm for the width.

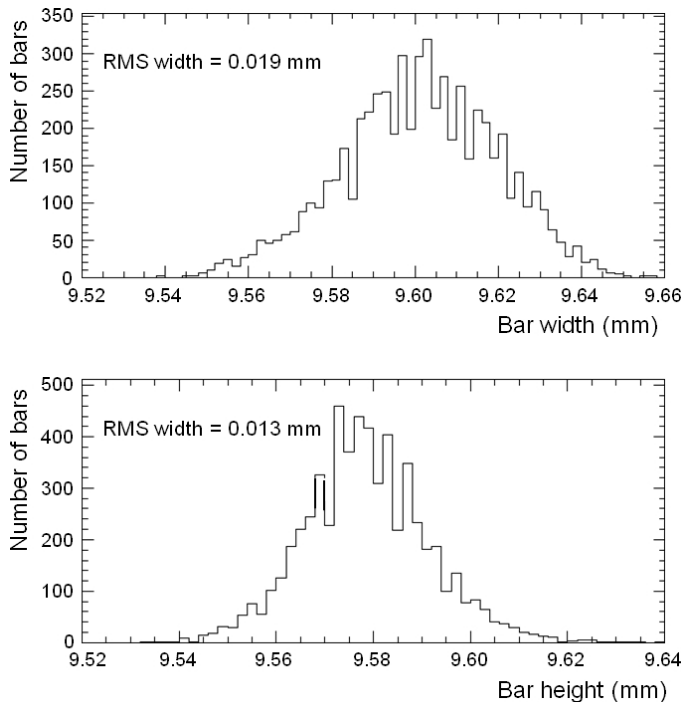


Figure 4: Measured distributions of the mean widths and heights of the bars. Details of the measurements are given in the text.

#### 2.5. Bar scanner measurements

In order to look for dead spots (areas of the bar which scintillate less than the rest of the bar) and to compare light yields among the bars as they came off the production line, the bars were scanned by moving a  $^{106}\text{Ru}$  beta source along the length of a bar. The light output from a WLS fiber threaded through the hole in the bar was measured with an unbiased photodiode whose current was read out by a Keithley picoammeter. When looking for dead spots, measurements were made every 2 cm; when comparing light yields between bars they were made every 50 cm. A special table and computer controlled movable source holder were constructed so that these measurements could be carried out reproducibly. The same fiber was used throughout. The results of a typical scan are shown in Fig. 5 together with an exponential fit to the data, which yields a normalized light yield,  $I_0$ . During production, about 1 in every 4 bars was scanned and the distribution of light yields was found to be Gaussian with a width of 4.5 %.

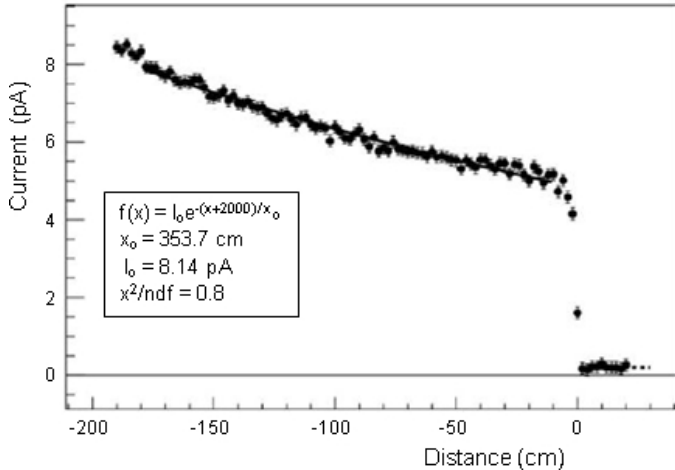


Figure 5: Normalized light yield from a typical bar scan. Measurements were taken with a  $^{106}\text{Ru}$  source placed at various locations along the bar. See text for details.

### 2.6. Light yield tests of bars

The M11 secondary beam channel at TRIUMF was used to measure light attenuation lengths and light yields from prototype scintillator bars extruded by Celco about 6 months before the main production run. The channel is described in Section 12.1. Electrons, muons and pions of 120 MeV/c were used and the light yield for each particle type was measured as a function of distance of the beam from the photosensor. For these tests a Russian (CPTA) silicon photosensor was used. The data are shown in Fig. 6.

Measurements with fibers with reflecting ends showed that the light yield at the end of the bar furthest from the sensor could be increased by 30-40 % by aluminizing the end of the fiber or by adding a reflecting cap. Thus aluminizing the far end of a fiber raised the expected light yield from the far end of the bar up to 16-18 photoelectrons (pe) for a minimum ionizing particle. For comparison, this level of light exceeds that seen in the SciBar detector, which saw  $\sim 16.5$  pe/cm for a minimum ionizing particle incident at the end *nearest* the photosensor [15].

### 2.7. Optical crosstalk

Optical crosstalk through the  $\text{TiO}_2$  coating between bars was investigated by measuring the amount of light seen in a bar when an adjacent bar was illuminated with 400 MeV/c protons or

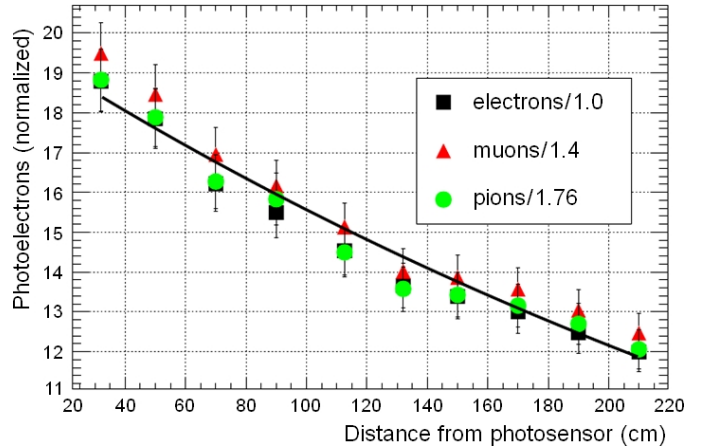


Figure 6: Light yield from a bar for 120 MeV/c particles read out with 1.0 mm Kuraray un-aluminized fiber and a Russian (CPTA) silicon photomultiplier photosensor, as a function of distance from photosensor. The data have been normalized by dividing the light yields by  $dE/dx$  for each particle relative to a minimum ionizing particle.

with an LED. The results of these measurements were consistent with each other and show that, with a  $\text{TiO}_2$  thickness of 0.25 mm,  $0.5 \pm 0.2$  % of the light produced in one bar is transmitted through the coating into an adjacent bar.

Because the FGD uses one photosensor per fiber, there is no crosstalk between scintillator bars inside the photosensors themselves.

### 2.8. Aging tests

Fermilab estimated that aging of bars produced for MINOS would reduce the light yield by  $\sim 2$  % per year [16]. To check for aging of our bars, we exposed a scintillator bar and wavelength-shifting fiber to a  $^{90}\text{Sr}$  source and measured the light yield with a photodiode, comparing our bars to samples of Fermilab bars with both at room temperature. We also attempted to accelerate the aging by heating samples of the bars in an oven to 45 °C, 60 °C and 85 °C. The results of these tests may be summarized as follows:

1. Scaling the 60 degree and 85 degree aging rates with the Arrhenius equation predicted a loss of light output of  $\sim 0.2$  % a day or 75 % in a year. These results were rejected because the temperature was too close to the scintillator glass transition temperature.

2. A light loss of  $\sim 3.93 \pm 1.60$  % per year was obtained directly from the room temperature data in Fig. 7 top.
3. A loss of  $\sim 1.93 \pm 0.25$  % per year was predicted from using the Arrhenius scaling rule to the 45 degree data in Fig. 7 top.
4. The change in the ratio between the light output of the TRIUMF bars and the Fermilab bars at room temperature over a 250 day period is consistent with zero (see Fig. 7 bottom).
5. The light output from 120 MeV/c muons measured over about a 1 year period showed no evidence of light loss.

The results of 2), 3) and 4) are all consistent with an aging rate of about  $\sim 2$  % per year, the same as obtained by Fermilab [16].

### 3. XY Module assembly

Each XY module is a glued sandwich consisting of 192 active scintillator bars in the  $x$  direction glued to 192 active bars in the  $y$  direction. Skins of 0.25 mm thick G10 (obtained from Current Inc.) are glued to both the upstream and the downstream surface of the XY module to provide additional mechanical rigidity and to allow handling of the modules without stressing the glue joint between the  $x$  and  $y$  layers. Each layer of an XY module actually contains 194 bars, but the top edge of the outermost bar on each side is machined off to provide a surface for mounting the photosensor busboards to the scintillator layer. Thus the outermost bar does not contain a WLS fiber and is only half height. The outer dimensions of the module are 186.4 cm  $\times$  186.4 cm  $\times$  2.02 cm, not counting the photosensor busboards. The twenty-four photosensor busboards screw onto the four sides of the XY module and support the photosensors and fibers (see Fig. 19). Each XY module is supported from above by five stainless steel straps that wrap under the bottom of the module, attaching to mounting pads on the bottom of the module and to the top inner surface of the dark box (see Section 7.2).

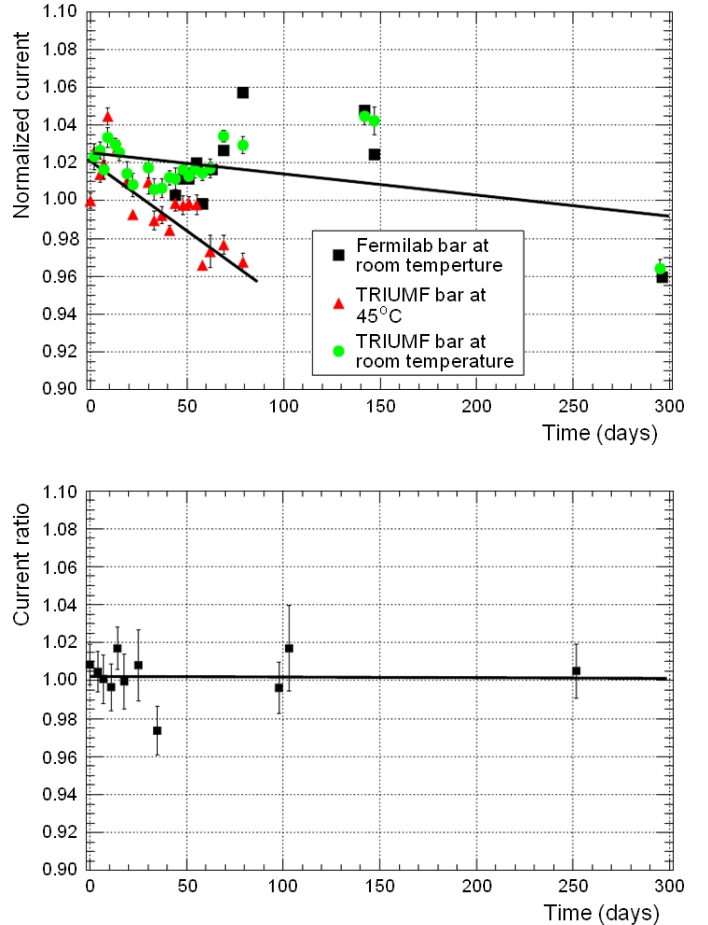


Figure 7: Scintillator bar aging study. (Top) Normalized photosensor current as a function of time from a scintillator bar exposed to a  $^{90}\text{Sr}$  source. (Bottom) Ratio of current from TRIUMF bar to current from Fermilab bar as a function of time.

#### 3.1. Glue tests

A large number of tests were carried out to find a suitable adhesive to bond the scintillator bars together. The desired adhesive needed to be able to adhere to both polystyrene and G10. The bonds also had to be resistant to peeling forces which might arise, for example, during handling of a glued layer of bars. Thus one test was a simple snap test in which two pieces of scintillator bar were glued together along part of their length and it was seen whether the scintillator or the bond joint failed when a torque was applied to the joint. A similar test was carried out in which a layer of G10 was glued to a scintillator bar to see if it was possible to peel the two apart. Many adhesives failed one or the other of these tests.

The other important characteristic of the ad-



hesive was that it needed to have a long enough working life that the component materials could be arranged in position before the glue set. Instant bonding type glues were not an option for our construction process.

A wide search of different types of adhesive to locate any likely candidates was carried out. Only two adhesives met all the requirements - Plexus MA560 and MA590 (obtained from ITW Plexus). Even for these glues it was found that although they had satisfactory strength and pot life, they lost strength rapidly from the time they were prepared if not applied promptly (they are two-part adhesives), so much so that within 10 to 15 minutes they both failed the snap test described above. We chose to use MA590 since it had a longer pot life, but nevertheless it was necessary to carry out the gluing procedure as quickly as possible.

### 3.2. Assembly procedure

The XY layers were assembled in the largest TRIUMF Detector Facility clean room. There were three separate bonding steps in which first one layer was glued, then the second, and finally the two were bonded together. The procedure for bonding an individual layer was to align 196 bars in a jig on a granite table, apply adhesive to the top side of the G10, then flip it over and lay it on top of the bars. Slightly wider bars were paired with slightly narrower bars to avoid tolerances from wider or narrower bars from accumulating. Before applying adhesive, the bar codes were scanned and stored in a database. Thus the location of each particular bar in the FGDs is known. Also note that no adhesive was applied between the bars. The G10 sheet was actually composed of two separate sheets, each covering half of each bar, for ease of handling. When the G10 sheets were in place, an aluminum cover plate was placed on top of the layer, four aluminum I beams were placed over the plate and attached by turnbuckles to a hydraulic system that was activated to pull down on the beams, providing pressure while the glue set. The whole procedure took less than 15 minutes from the moment the glue was mixed. The bond was allowed to set

overnight. See Fig. 8 for a photo of a layer lying on the granite table with the pressure applied.

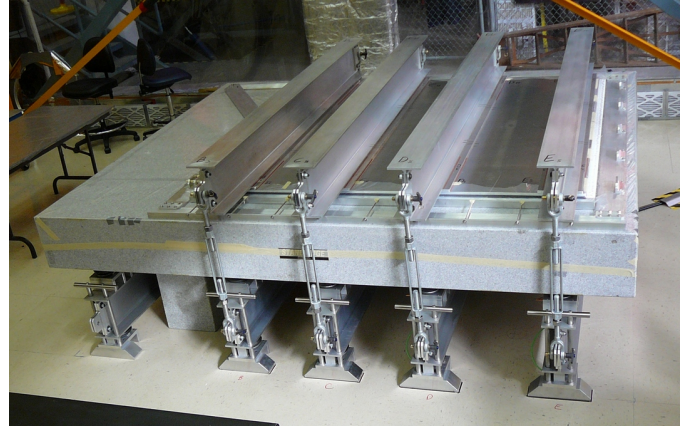


Figure 8: A layer of scintillator bars after the glue has been applied, the G10 laid over top, the cover plate and I beams put in place and hydraulic pressure applied.

The procedure for bonding one layer to the other was to set one layer into the jig, scintillator side up, and apply a layer of adhesive to the exposed bars. Then the other layer was craned over top, scintillator side down and with the bars aligned at  $90^\circ$  to the other layer. The jig ensured the layers remained at right angles as the top layer was lowered. Finally the aluminum plate, I beams and hydraulic system were deployed as before.

### 3.3. Final preparation

Upon completion of the gluing procedure, the module was moved to a router table for machining to final dimensions. The same router was used as is described in [7]. First, the outermost bar on all four edges of the module was machined off. Then the top half of the next bar on all four edges was removed to provide a surface for attachment of the bus boards, and the screw holes to hold the boards were drilled. Finally, the module was deburred by hand to remove any sharp edges.

After the photosensor bus boards and daughter cards were mounted, the WLS fibers were slid through the holes in the bars and attached to the MPPCs. A ferrule was pre-glued onto one end of each fiber so that it was only necessary to slide the ferrule into a coupler in front of the MPPC (see Fig. 15). Finally, the stainless steel straps from which the XY module hangs were attached at five

locations across the bottom of the FGD module. The XY module was then ready for installation inside an FGD dark box (see Section 7).

### 3.4. Elemental composition

The elemental composition of the modules was determined from the measured geometry of the scintillator bars and their known composition, and the measured amounts of MA590 and G10. The compositions of the latter two materials are not known precisely but under reasonable assumptions the uncertainties do not contribute significantly to the overall uncertainty of each element. A consistency check was made by weighing the modules after machining and by taking account of the material that had been removed, the areal density agreed with that calculated from the individual components within 0.5 %.

After final assembly it was also necessary to take into account the contribution from the wavelength shifting fibers. These were assumed to be composed of 100 % polystyrene.

The final areal densities of each of the elements contained in the modules are presented in Table 5 in Section 6.

## 4. Wavelength shifting fibers

The WLS fiber chosen was a 1 mm diameter, double-clad Kuraray Y11 (200) S-35 J-type fiber. In these fibers, the peak absorption wavelength is 430 nm and the subsequent emission spectrum is peaked at 476 nm. The capture and transmission of light in the fiber are improved with double cladding with the following indices of refraction: 1.59 (core); 1.49 (inner clad); 1.42 (outer clad). S-type fibers are mechanically stronger at some expense to the light transmission.

Twenty-one kilometers of WLS fibers were obtained from Kuraray in 2.1 m lengths. Random samples of the fibers representing 10 % of the total were visually inspected for physical defects upon receipt. The diameter of the fibers were found to be  $1 \text{ mm} \pm 2 \%$ , consistent with the Kuraray specifications. Only 0.80 % of the inspected fibers were found to have some problem.

Subsequently, the fibers were sent to the Fermi National Accelerator Laboratory (FNAL), where one end of each fiber was mirrored for enhanced light collection. The mirroring technique consists of aluminizing the fiber end by vacuum thin-film sputtering deposition, and then coating with Red Spot UVBT115R5, a one-part epoxy that cures with UV, for protection. The epoxy extends about 0.15 mm from the fiber end, while the radial thickness with respect to the surface of the fiber is less than 0.1 mm. Preliminary measurements with pions, muons and electrons using the M11 test beam facilities at TRIUMF demonstrated a substantial gain in the light yield for pulses originating at the mirror end of the fiber, after mirroring the fibers (see section 2.6).

Upon their return from FNAL, the mirrored fibers were cut and polished to a length of 191.5 cm. Subsequently their attenuation properties were measured with a custom fiber test device (see section 4.2). Half the fibers were tested after the FGD fiber-MPPC coupler (described in section 5.3) was glued onto the unmirrored end, and half were tested before the coupler was glued on. The two groups of fibers were analyzed separately; the fibers measured before the connector was glued on are designated as group 1 fibers and those measured after are designated as group 2 fibers.

### 4.1. Preparation

A cutting jig was built to shear the fibers slightly longer than the required 191.5 cm. After shearing, a FiberFin model FF4 diamond fiber polisher was used to cut and polish to within 1 mm of the specified length.

A CCD camera looking through a measuring microscope was used to inspect the fiber end and to verify the length of the finished fiber, which could easily be measured to within 0.1 mm.

Bicron BC600 glue was chosen to fix the coupler to the fiber. This glue was selected because of its characteristics - bond strength, curing time (workable for about 4 hours at 21 °C), slow aging effect, etc. - and also because it is intended to be used with optical fibers, and therefore is not expected to harm the fibers chemically.

A gluing jig was developed to ensure the fiber ends were flush with the coupler end so that the gap between fibers and light sensors is minimal and reproducible (see Fig. 9). In order to avoid glue flowing towards the fiber end or out of the coupler, the glue was allowed to react for approximately two hours before use in order to increase its viscosity. An EFD Ultra 2400 Glue Dispensing workstation was used to provide appropriate small quantities (0.05 ml of this glue mix) to each fiber, before insertion into the coupler in the jig. After 24 h curing time, every glue joint was tested for strength to withstand 0.5 N force (more than the force required to remove a coupler from the detector).

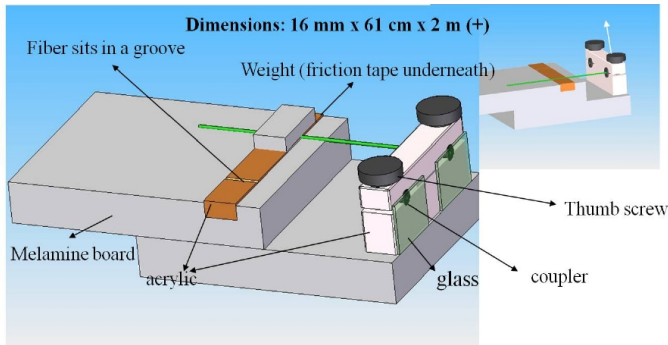


Figure 9: Schematic diagram of the jig used to glue the couplers to the end of the fibers.

#### 4.2. Fiber tests

All fibers used in the FGDs were tested after mirroring. The fiber tester is comprised of light sources, light detectors, mechanical support for the fibers, computer control, multiplexer and a picoammeter.

The light sources are nineteen 1.5 candela, 5 mm diameter UV light-emitting diode (LED) assemblies. In each assembly, the LED emits light into five clear fibers which fan out to inject light throughout a piece of FGD scintillator bar whose dimensions are 1 cm  $\times$  1 cm  $\times$  10 cm. A sixth clear fiber was routed from each LED to a common large area silicon pin-photodiode to monitor and correct for LED light intensity variations. There are ten grooves cut perpendicular to the long axis of the scintillator bar that serve to hold the fibers being tested. The assemblies are located

at 10 cm intervals along a dark box. Darkened aluminum plates fix the spacing between the bars and support the fiber at the height of the bottom of the grooves. The arrangement of the LED assemblies is shown in Fig. 10.

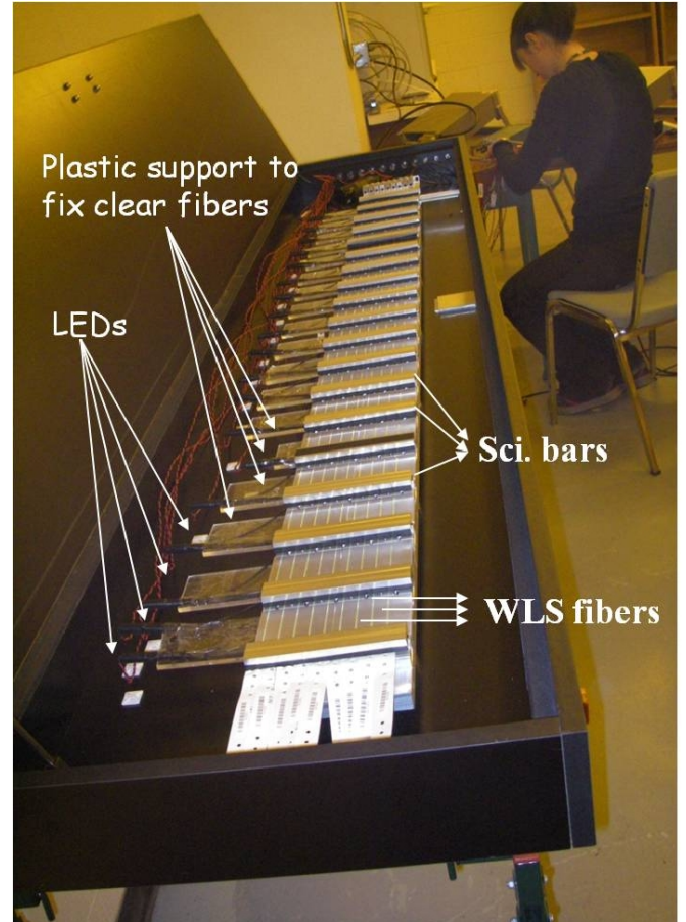


Figure 10: Photo of the fiber tester, showing several light sources and their corresponding fiber optics and grooved scintillator bars.

An SHE Corporation constant current power supply (CCS) was used to drive the LEDs, one at a time. It was found that LED lifetime was prolonged when the pattern to turn an LED off or on included steps where the LED was switched while in parallel with a dummy load to minimize the voltage swing of the CCS.

Ten light-detector elements were positioned to couple to the fibers in the grooves. The detector elements were arranged with Ocean Optics bare-fiber couplers for all group 1 measurements (when testing preceded gluing) and with standard FGD fiber couplers for all group 2 measure-

ments (when gluing preceded testing). In either case, each channel was instrumented with a Hamamatsu S1336-18BQ silicon pin-photodiode, and typically nine of these channels were used, so that a separate data channel with a constant WLS fiber was available as reference for normalization purposes at all times.

Calibration of the system was necessary to compensate for variations in the fiber-to-groove optical coupling at every measuring location. This was accomplished using a short segment of fiber attached to a single, movable detector, used at every LED-groove intersection, one at a time.

Operation of the tester was fully computer controlled using a GPIB interface and Keithley 7001-S control mainframe with Keithley 7058 scanner cards to switch both LED power and photodetector channel. Under program control, one LED would be turned on and one fiber channel read out at a time. The current from each light detector was determined with a Keithley 6487 picoammeter, operating with sampling and filtering. Measurements were repeated and data written to disk for later analysis. The reproducibility of the measurements was found to be improved when the LEDs were cycled at the same rate as in data taking at all times, even between measurements.

#### 4.3. Attenuation analysis

A typical attenuation curve for a mirrored fiber after data calibration and LED light variation correction is shown in Fig. 11. The attenuation curve can be empirically described using equation 1:

$$I = A e^{-x/L} + B e^{-x/S} \quad (1)$$

where  $L$  and  $S$  are referred to as the long and short light attenuation lengths respectively, and the ratio of  $B$  to  $A$  indicates the relative contribution of each term. In this expression,  $I$  is the current from the photodetector and  $x$  is the distance from the source to the light detector.

The attenuation lengths and mean values of  $A$  and  $B$  are given in Table 1.

There were strong correlations among  $L$ ,  $S$ ,  $A$  and  $B$  such that they are not robust parameters to test the quality of fibers. On the other hand,

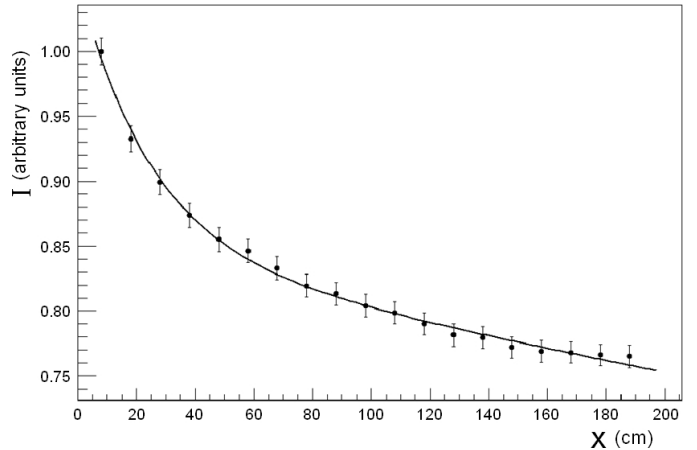


Figure 11: A typical attenuation curve for a mirrored fiber. The data are fit using equation 1.

Table 1: Values of the long and short attenuation lengths and their amplitudes for the two groups of fibers.

	$L$ ( $\sigma_L$ ) (m)	$S$ ( $\sigma_S$ ) (m)	$A$ ( $\sigma_A$ ) (nA)	$B$ ( $\sigma_B$ ) (nA)
group 1	16.0(3.2)	0.236 (0.042)	1.47(0.08)	0.45(0.04)
group 2	16.0(3.1)	0.258(0.041)	1.19(0.06)	0.27(0.03)

variables such as the ratio  $B/A$  and the comparative light yield relative to the reference fiber are of particular interest to the quality control of the fibers as they are expected to be constant from fiber to fiber. These two distributions are shown in Figs. 12 and 13. The comparative light yield is the average over all 19 ratios of yield in an individual fiber being tested to the corresponding yield for the reference fiber. Numerical values are given in Table 2.

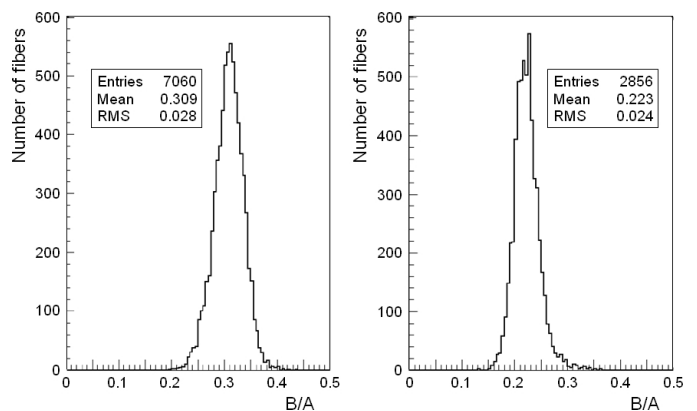


Figure 12: Distribution of the ratio  $B/A$  for data group 1 (left) and data group 2 (right).

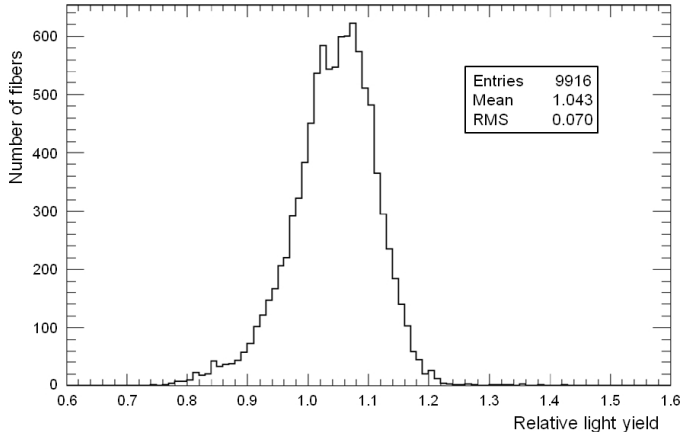


Figure 13: Combined distribution (groups 1 and 2) of the relative light yield between the tested and reference fibers.

Table 2: Ratios of the amplitudes for the long and short attenuation lengths for the two groups of fibers and the overall light yield relative to the reference fiber.

	mean	RMS	RMS/mean (%)
$B/A$ (group 1)	0.309	0.028	8.98
$B/A$ (group 2)	0.223	0.024	10.9
Relative light yield	1.043	0.070	6.72

Only 46 fibers were finally rejected on the basis of one or more cuts on the ratio of light output to that of the reference fiber (25 failed), chi-square of the fit to the attenuation curve (15), ratio  $B/A$  (7), and the long and short attenuation lengths (17 and 13, respectively) [17].

## 5. Photosensor

The photosensor for the FGDs needs to satisfy tight constraints:

- It must be able to count photons down to a few photoelectron level.
- It must work in the 0.2 T magnetic field.
- It must fit in a very tight space constraint.

The Multi-Pixel Photon Counter, or MPPC [12, 13], manufactured by Hamamatsu Photonics [18], meets all these requirements and was chosen for all the scintillator detectors in ND280, including the FGDs.

### 5.1. MPPC description

The MPPC is a pixellated avalanche photodiode (APD) that operates in Geiger mode. A picture of the MPPC used (S10362-13-050C) is shown in Fig. 14 and the major specifications are summarized in Table 3. The outer dimensions of the package are 5 mm  $\times$  6 mm. The sensitive area of the MPPC is enlarged from the 1  $\times$  1 mm<sup>2</sup> of those shown in the catalog to 1.3  $\times$  1.3 mm<sup>2</sup> to minimize the light loss at the optical contact. The size of one APD pixel is 50  $\times$  50  $\mu$ m<sup>2</sup> and the number of APD pixels is 667. A single pair of leads provides for both the operating voltage and signal readout.

For an MPPC, each APD pixel independently works in limited Geiger mode with an applied voltage just above (usually  $< 1$  V) the breakdown voltage ( $V_{bd}$ ). When a photoelectron is produced, it induces a Geiger avalanche that is passively quenched by a resistor integrated to each pixel. The output charge  $Q$  from a single pixel is independent of the number of produced photoelectrons within the pixel, and can be written as  $Q = C(V - V_{bd}) \equiv C\delta V$ , where  $V$  is the applied voltage and  $C$  is the capacitance of the pixel. The overvoltage,  $\delta V \equiv V - V_{bd}$  is the key parameter that controls the performance of MPPCs. Combining the output from all the pixels, the total charge from an MPPC is quantized to multiples of  $Q$  and proportional to the number of pixels that underwent Geiger discharge. The number of discharged pixels is proportional to the number of incident photons if the number of incident photons is small compared to the total number of pixels. Thus, the MPPC has an excellent photon counting capability as long as the number of photoelectrons does not approach the total number of pixels in the device. The MPPC is particularly suitable for the FGDs because of its excellent photon counting capability with higher quantum efficiency than photomultipliers for the wavelength distribution produced by the WLS fibers.

### 5.2. MPPC tests

All the MPPCs used in the FGDs were tested before integration with the detectors. The details of the procedure and the results are described

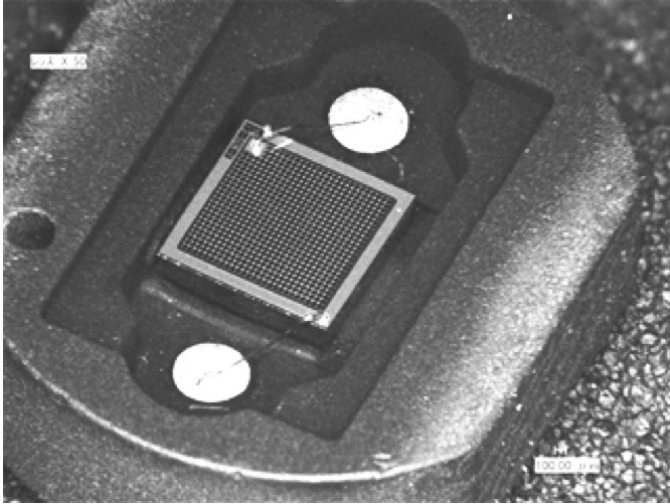


Figure 14: Picture of MPPC developed for T2K.

Table 3: Specifications of T2K-MPPC (S10362-13-050C).

Item	Spec.
Active area	$1.3 \times 1.3 \text{ mm}^2$
Pixel size	$50 \times 50 \text{ } \mu\text{m}^2$
Number of pixels	667
Operation voltage	70 V (typ.)
PDE @ 550 nm	>15%
Dark count [ @ 25 °C ]	(>0.5 pe) <1.35 Mcps (>1.2 pe) <0.135 Mcps

in [19]. In order to characterize a large number of MPPCs, a system was developed that simultaneously measures 64 MPPCs with various bias voltages and temperatures. The gain, dark noise rate, photodetection efficiency (PDE), crosstalk and after-pulsing probability of 17,686 MPPCs (including those to be used for other detectors in ND280 besides the FGDs) were measured as functions of the operating voltage and temperature.

Table 4 summarizes the mean value and RMS of measured performance for these MPPCs at 20 °C and  $\Delta V = 1.0V$ . All the measured MPPCs satisfy the requirements for the FGDs.

### 5.3. Coupling to WLS fiber

In order to achieve good optical coupling between a WLS fiber and an MPPC, a custom connector was developed [20]. As shown in Fig. 15, the connector consists of two parts: one part holds the MPPC at the bottom of the funnel (right), and the other part is glued to the fiber (left). The two parts can be latched together without glue

or screws but just by a mechanical force so that the connection is simple while well-aligned and robust. The outer dimensions of the coupler are about 8 mm in diameter and 17.5 mm in length when the two parts are connected, fulfilling the space constraint from the mechanical design.

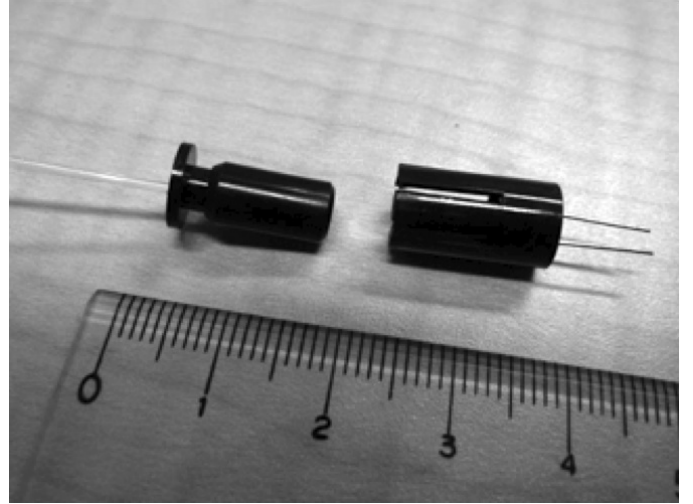


Figure 15: Coupler to connect MPPC (right) and WLS fiber (left).

The light loss due to coupling was measured with this coupler, a 1 mm diameter WLS fiber, and a prototype MPPC with a  $1 \times 1 \text{ mm}^2$  active area. The measured light loss was 13 % [20]. The light loss with the final MPPC is expected to be less than this because of the enlarged active area.

## 6. Target water system

The second FGD alternates scintillator modules with  $\sim 25 \text{ mm}$  thick polycarbonate panels containing water [21]. These panels, maintained under subatmospheric pressure to prevent water leaks, serve as targets for studying neutrino interactions on water. The panels are constructed so that their elemental compositions nearly exactly match those of a mixture of water and polystyrene scintillator, allowing the total interaction rates on water to be determined by measuring the total interaction rate in FGD2 and subtracting out the interaction rate on polystyrene as measured in FGD1.

Table 4: Mean value and RMS of gain, dark noise rate, after-pulsing and cross talk probability, and photodetection efficiency (PDE) for 17686 MPPCs at 20 °C and  $\Delta V=1.0 V$ .

Parameter	Measured values	RMS	Value/RMS (%)
Gain	$4.85 \times 10^5$	$0.26 \times 10^5$	5.4
Breakdown voltage (V)	68.29	0.73	1.1
Dark noise rate (Hz)	$4.47 \times 10^5$	$1.02 \times 10^5$	22.8
After-pulsing and cross talk probability	0.070	0.036	51
Relative PDE ( $\times$ PMT)	1.53	0.33	22

### 6.1. Water panel description

The water modules for the FGD were built from rigid, hollow polycarbonate panels, originally designed for use as wall material for greenhouses. These corrugated panels are 25.4 mm thick, 1809 mm wide, and are extruded in long sections that are cut to length. The panels were constructed from Sunlite<sup>®</sup> polycarbonate multi-wall sheets produced by the Palram company. Polycarbonate is a strong, lightweight, waterproof material ideal for making water panels. The panels are divided into long cells by regular internal walls that provide rigidity and strength and also help to maintain the shape of the panel and prevent bulging even when filled with water. Furthermore, their oxygen content is such that it permits matching the elemental compositions of a water-filled panel with a mixture of water and polystyrene scintillator.

Figure 16 shows a schematic view of the internal wall structure of a panel. The long internal cells of the panel are oriented vertically inside the detector, and water continuously flows in the bottom and out the top under the control of the sub-atmospheric pressure system.

Two water panel productions were done using slightly different models of polycarbonate panel. The first six panels were produced using a slightly heavier panel thickness, while another three panels were produced using a marginally lighter panel. Ultimately the best six panels were deployed in the detector, including five from the first production run and one from the second run, with the other three panels retained as spares.

#### 6.1.1. Panel fabrication

The panels as delivered from the supplier were first cut to a specified length. For the first pro-

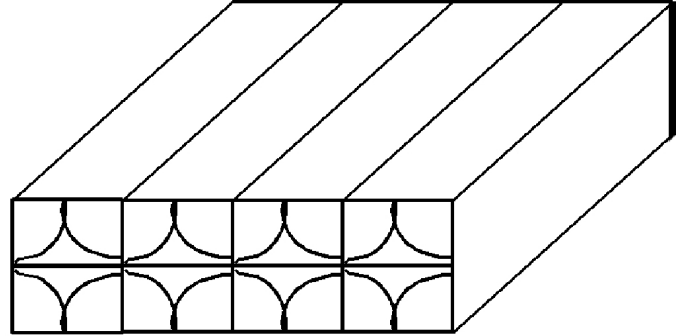


Figure 16: Cross-sectional view of a section of a polycarbonate water module panel, showing the internal wall structure. The approximate panel thickness is 25.4 mm. Drawing is not to scale.

duction of water modules, the panels were cut to a length of 1873 mm, while for the second production this was modified to 1863 mm.

After the panels were cut, the next step was to pierce the inner walls of the panel at each end to create a contiguous internal volume that could be filled and drained through a single inlet and outlet. Each of the thin walls (round walls in Fig. 16) had a horizontal slot cut in it using a Dremel multi-tool and then a vertical slash cut with a sharp pick to produce a T-shaped opening, while the thick internal walls each had two round holes drilled in them with the Dremel. These holes allow water to flow from one adjacent vertical cell of the panel into its neighbors. All of these cuts were made 1.5-2 cm from the edge of the panel to allow room for the sealant.

Each end of the polycarbonate panel was sealed with a polyurethane sealant<sup>1</sup>. This sealant was chosen for its compatibility with polycarbonate, its low level of absorption of water, and a low probability of its curing process damaging the

<sup>1</sup>HE1908, obtained from Engineering Chemicals B.V.

polycarbonate substrate. Prepared sealant was poured evenly into a high-walled, tight-fitting channel, then the end of the panel was fitted into the channel to immerse the end in sealant. This sealing process produces solid seals extending 1-1.5 cm into the body of the panel. Brass fittings inserted through the polyurethane seal in the bottom right and top left parts of the panel provide input and output ports, respectively.

### 6.1.2. Elemental composition

Polycarbonate has a chemical formula of  $C_{16}H_{14}O_3$ . Subtracting the equivalent of three water molecules from its composition leaves a remainder of  $C_{16}H_8$ . To match the C:H ratio of the residual material to polystyrene,  $(CH)_n$ , thin sheets of polypropylene,  $CH_2$ , were glued to the front and back surfaces of each panel. Two sheets of 0.8 mm thick polypropylene were attached to each panel with thin layers of CLR 1390/CLH 6025 epoxy (obtained from Crosslink Technology Inc.). Thirty thin 25.8 mm  $\times$  51.6 mm G10 plastic spacers were then attached to each side of the panel to provide spatial separation between each module and its neighbor when hanging inside the FGD. The total thickness of a panel, including polypropylene skins and spacers, is 30.0 mm.

The areal mass densities of all components were measured and used to compute the elemental compositions per unit area for each panel. Table 5 shows the composition for Panel 0. Also shown is the composition of an XY module. The final row shows the leftover material if the scintillator module composition, scaled by the relative amounts of carbon in a water panel and a scintillator module, is subtracted from the water panel composition. Essentially the equivalent amount of “scintillator-like” material and  $H_2O$  in the panels are determined by the carbon and oxygen contents, respectively, with the “remainder” representing the total material left over after the subtraction. The full water panel is shown to be equivalent to 490 mg/cm<sup>2</sup> of scintillator-like material, 2297.2 mg/cm<sup>2</sup> of water, plus a few mg/cm<sup>2</sup> of trace amounts of H, Mg, Si, and Ti that do not cancel in the subtraction. These results demon-

strate that the elemental composition of the panels is carefully tuned so that each water panel is compositionally equivalent to a mass of pure water and a mass of scintillator module material.

### 6.2. Subatmospheric pressure system

A schematic of the water system is shown in Fig. 17. The system is designed to maintain the pressure of FGD water vessels inside the magnet below atmospheric pressure to prevent water emission through any leaks that may arise. Any leak results instead in only ingress of air; a substantial rate of ingress can be tolerated by the system while still maintaining effective operation. The water panels are rigid enough that they can sustain full vacuum in principle, although the system and operating procedures are designed to limit the pressure in the panels to greater than 200 mbarA in all conditions. There was insufficient space in the dark box to install level sensors in the panels or for buffer tanks above them to contain sensors. Hence, the principle for ensuring that the panels remain full is to maintain upward water flow at all times at a flow rate that is somewhat less than 1 L/min. Flow to the inlets at the bottom of panels (about 3.8 m from the floor) starts from an open reservoir on a 2.4 m high stage, with a maximum water level just below the lowest water connection inside the magnet that might leak. A typical operating water level in the reservoir is 3 m from the floor. Flow results from the connection of the outlets at the tops of the panels to a vacuum vessel at floor level, with a typical half-full operating water level of about 1 m from the floor. The operating pressure in the vacuum vessel is 300 mbarA, which is maintained by a closed loop servo controller driving a proportional valve leading to a vacuum buffer tank. A humidity-tolerant vacuum scroll pump runs whenever needed to keep this buffer tank at a lower pressure. The water level in the vacuum vessel is maintained by a closed loop servo controller driving a water pump that returns water from this vessel to the overhead reservoir. This water pump is a conventional centrifugal type, but with parameters selected conservatively to avoid cavitation on the impeller despite the low suction



Table 5: Elemental composition of Water Panel 0. All entries are in units of mg/cm<sup>2</sup>. The first three rows give the amounts of each element for an empty water panel, for the water inside it (for Panel 0), and the total. The fourth row lists the elemental composition of an XY scintillator module. The last three rows show how the composition of the full panel can be decomposed into the sum of a mass of scintillator module-like material, of water, and of a remainder.

	C	O	H	Mg	Si	Ti	Total
Empty panel	422.0 ± 6.9	92.7 ± 3.6	43.6 ± 0.9	6.8 ± 0.9	11.2 ± 1.4	0	577.2 ± 12.5
Water in panel 0	0	1967.4 ± 3.3	248.0 ± 0.4	0	0	0	2215.4 <i>pm</i> 3.7
Panel 0 (full)	422.0 ± 6.9	2060.1 ± 4.9	291.6 ± 1.0	6.8 ± 0.9	11.2 ± 1.4	0	2792.6 ± 13.4
XY Module	1848.6 ± 9.2	79.4 ± 4.8	157.9 ± 2.1	0	21.8 ± 4.3	35.5 ± 5.9	2146.3 ± 14.4
“XY”-like	422.0 ± 6.9	18.1 ± 1.1	36.0 ± 0.8	0	5.0 ± 1.0	8.1 ± 1.4	490.0 ± 9.0
H <sub>2</sub> O	0	2042.0 ± 5.0	255.4 ± 0.6	0	0	0	2297.2 ± 5.7
Remainder	0 ± 9.8	0 ± 7.1	1.2 ± 1.4	6.8 ± 0.9	6.2 ± 1.7	-8.1 ± 1.4	5.4 ± 17.1

pressure. Each of the six water panels has its own independent flow loop so that they can be filled or drained independently. Each loop contains a flow meter, as well as a 3-port valve in both the supply and return legs, which are used to fill and drain the panel without risk of positive pressure in the panel at any time, even if there are in-leaks of air. Draining occurs in the reverse flow direction, and involves the slow metered admission of air to the top of the panel to maintain subatmospheric pressure in the panel. The water temperature is controlled by a heat exchanger that also carries coolant flow from the detector cooling system. A small amount of antimicrobial and anticorrosive agents (0.25 % by volume of liquid Germall Plus, manufactured by Sutton Laboratories, plus 10 ppm tolyltriazole) dissolved in the water inhibits biological growth in the system.

## 7. Dark Box

The scintillator and water modules hang inside a lighttight structural framework known as the dark box. Each dark box has external dimensions of 2300 mm × 2300 mm × 365 mm thick along the beam direction, with internal dimensions of 2069 mm × 2069 mm × 352 mm. Inside the dark box are the scintillator modules with their associated WLS fibers, photosensors on busboards, and the water modules. Front-end electronics cards are mounted around the four sides of the dark box, outside the lighttight volume. Twenty-four backplanes mounted along the four sides of the dark box (six per side) provide the connection between the photosensors on busboards inside the

lighttight region and the electronics cards on the outside. Thin aluminum cover plates on the upstream and downstream faces of the dark box complete the lighttight enclosure. A water cooling system operated at subatmospheric pressure cools the exterior electronics. Each dark box weighs 327 kg, not including the electronics cards, and is made almost entirely of aluminum.

### 7.1. Construction

The main structural elements of the dark box frame are

1. eight long aluminum I beams that fit together to form upstream and downstream square frames, each with outer dimensions of 2300 mm × 2300 mm
2. four side plates for the top, bottom, left and right sides of the FGD, which bolt to the insides of the upstream and downstream I beam frames and contain cutouts for the backplanes
3. thin square aluminum front and back covers that mount on the upstream and downstream faces of the FGD
4. cross braces across the top face of the FGD from which the modules inside the dark box are suspended

A photograph of the FGD frame is shown in Fig. 18. The aluminum I beams that form the dark box frame are machined out of 104.3 mm × 50.15 mm bars of solid aluminum. Material is removed from either side to leave a web of thickness 4.15 mm, except for regions near the end,

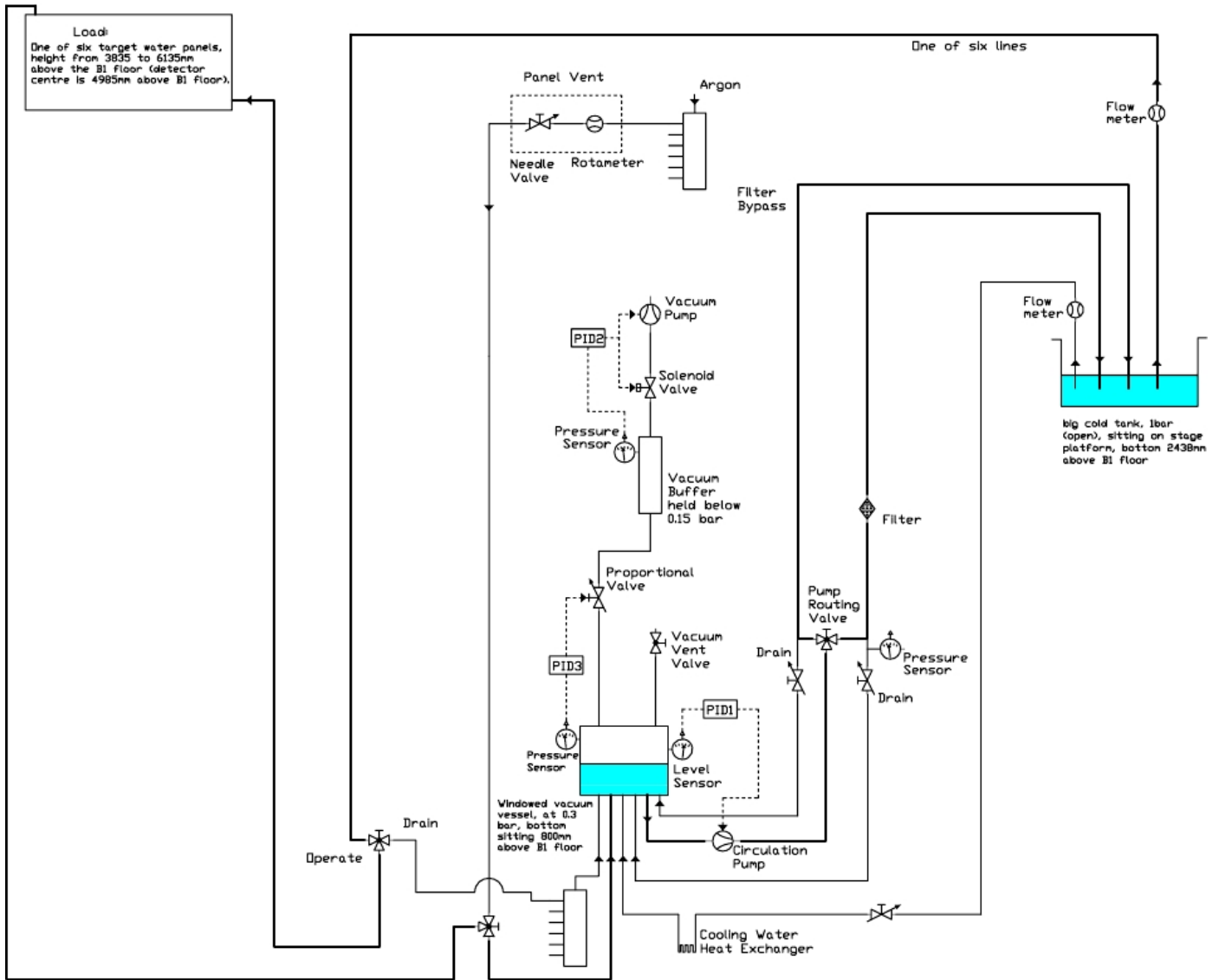


Figure 17: Schematic of the subatmospheric pressure water system.

thereby reducing the weight by  $\sim 65\%$ . Four I beams fit together to form a square frame on the upstream end of the FGD, while the other four form a similar frame on the downstream end. Four  $M12 \times 150$  mm stainless steel bolts join the I beams at each corner where the beams are solid without any material removed. The I beam flanges on the inner side of each square frame mount to the side plates while the outer flanges define the outer surface of the FGD. The distance along the beam direction between the outer edges of the upstream and downstream cover plates is 365 mm. The four vertical I beam members extend 35 mm below the bottom edge of the FGD,

forming “feet” to which mounting hardware is attached.

The four side plates consist of 11.2 mm thick aluminum plates that are 348.2 mm long in the beam direction, which when bolted to the inner surfaces of the I beam frames form an enclosed area with internal dimensions of 2069 mm high by 2069 mm tall. Each side plate is bolted to the upstream frame along one long edge and to the downstream frame along the other. Six rectangular cutouts ( $166 \text{ mm} \times 258.5 \text{ mm}$ ), equally spaced along the length of each side plate, provide space for mounting lighttight electronics backplanes. Signals from photosensors are carried

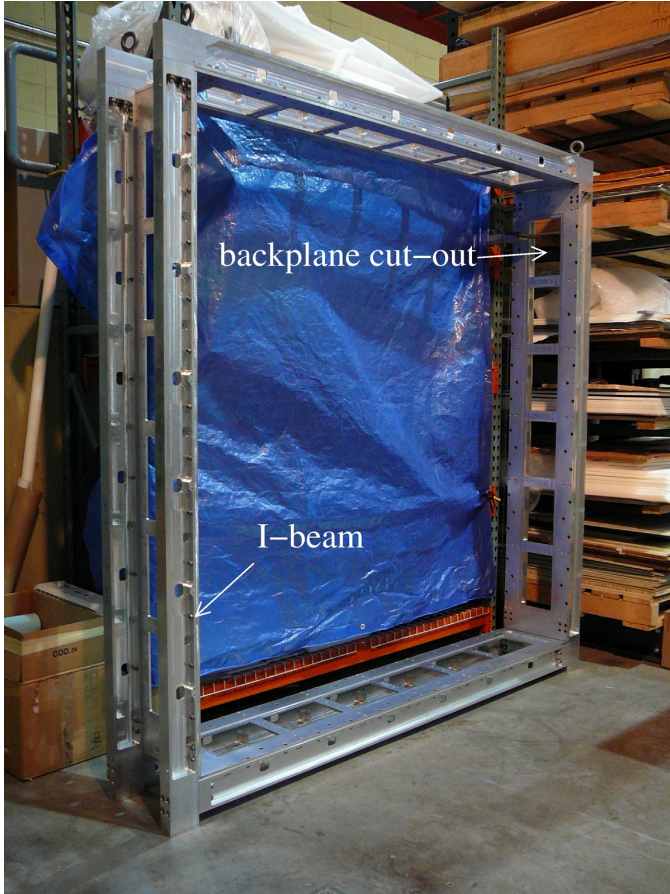


Figure 18: Photograph of the dark box structure. One of the 24 cutouts for backplanes and one of the 8 I beams are labelled.

by ribbon cables from busboards inside the dark box to the inner surface of the backplanes (see Fig. 19), while their outer surfaces present connectors that front-end electronics cards plug into. These cards reside in the 104.3 mm tall region between the outer edge of the I beam frame and the outer surface of the side plate.

The upstream and downstream aluminum cover plates are square, with a 6.4 mm thickness around the edges and a 1.6 mm thickness over the central  $1856 \times 1856 \text{ mm}^2$  area. They are attached to the I beam frames around their perimeter with small screws, with black PORON<sup>®</sup> stripping along the edge to ensure a lighttight seal.

Five steel crossbars, spaced evenly across the width of the FGD and oriented in the beam direction, attach to the inner top side of the dark box and provide structural support for the XY

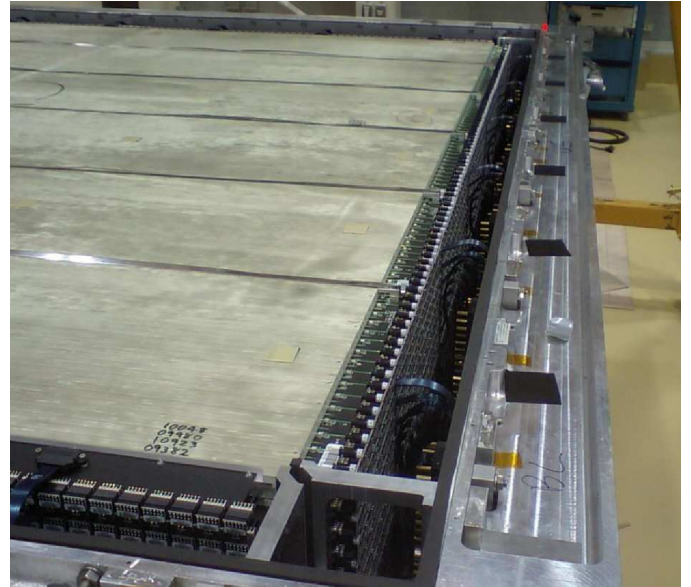


Figure 19: Photograph of the XY modules inside the dark box. Busboards carrying photosensors are mounted along all four sides of each module. Ribbon cables connect each busboard to the backplanes (not visible in this photo) on the sides of the dark box. Angular support brackets in the corners of the dark box (bottom center of photo) prevent lateral movement of the XY modules within the dark box. The five stainless steel straps are also visible.

and water modules that hang from them inside the box.

Electrically isolated copper bars carrying low voltage power and ground run along the inside edges of the I beams, next to the backplanes. Trigger and signal cables run along the outer edges of the box, between electronics cards mounted in minicrates. The upstream and downstream walls of each minicrate contain slots to hold the cards in position in the minicrates. This arrangement is shown schematically in Fig. 20.

## 7.2. Module support system

In order to minimize the inactive mass inside the FGD fiducial volume, XY and water modules are suspended inside the dark box from thin stainless steel straps that loop under the bottom of each module and attach to the steel crossbars at the top of the box. Each module is supported by five 1 cm wide straps made of 0.025 mm thick stainless steel, spaced evenly across the width of the module. These straps loop around small alu-

minum pads mounted at the bottom of each module and are welded to top fixtures for attachment to the crossbars. Each top fixture is attached with a bolt to its crossbar, with Belleville washers mounted on the bolt to provide cushioning and accommodate small differences in strap tension.

Each crossbar itself has a threaded rod on its top that passes through holes in the top of the dark box to attach to a holding crossbeam on the outside of the box. Nuts at the top of these threaded rods lock the crossbars into position, and are adjusted so that the lengths of rod, and hence the vertical positions of crossbars, are equal.

### 7.3. Attachment to detector basket

The feet of each FGD rest on a narrow steel bar that is bolted to the inside bottom edge of the detector support basket. Large M16 bolts attach each foot to a bar, and thin aluminum shims are used to adjust the level of each foot. A support bracket attached to the top of each side of the FGD fits into an anchor mounted on the top rail of the basket. The support bracket is free to move up and down within the anchor bracket, allowing for possible sag of the basket under load, but prevents the top of the FGD from moving laterally.

### 7.4. Cooling system

A water circulation system operating at sub-atmospheric pressure cools the electronics in the minicrates. Chilled water flows through hollow aluminum extrusions mounted on the inside of each I beam. These extrusions are connected by hoses at the four corners to form two cooling loops: one on the upstream side of the FGD and another on the downstream side. Water flows clockwise through one loop and counterclockwise through the other. Fig. 20 illustrates the relative positions of the FGD electronics cards, I beam, backplane, and cooling and power bars inside a minicrate. Each electronics card in a minicrate carries an aluminum cooling plate mounted with a thermal coupling compound. Fingers on these plates fit into notches in a “cooling lid” that is bolted across the top of each minicrate in thermal contact with the two cooling bars on either side of it. Wire springs on a locking mechanism push

the card fingers into contact with the cooling lids. Thus heat is conducted from the electronics to the cooling plates, into the cooling lid, and hence into the cooling loops.

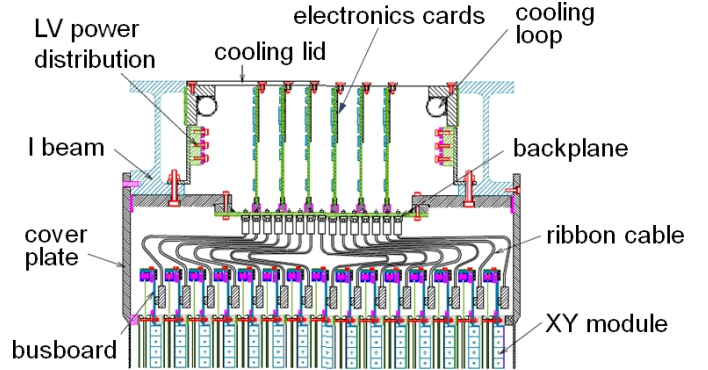


Figure 20: Cross-sectional view through a minicrate, showing the electronics cards, I beams, cooling and power bars, and backplane.

## 8. Electronics

The FGD readout electronics were designed to record a snapshot of the detector activity before, during and after the neutrino beam spill. The critical feature is the readout of the MPPCs by recording waveforms using switched capacitor array chips. The electronics provide both timing and energy (charge) measurement for all 8448 channels.

### 8.1. Requirements

The J-PARC neutrino beam structure is divided into spills of 6-8 bunches separated by  $\sim 580$  ns. The electronics must be active during each bunch. Furthermore, it is important to keep the electronics active between bunches and for several microseconds after the spill in order to tag Michel electrons from the decays of stopped pions. The total length of time recorded must therefore be close to  $10 \mu\text{s}$ .

The required charge resolution is driven by calibration demands. In order to calibrate the MPPCs, single pe peaks must be identified. Thus it is desirable to keep the electronics noise to a level less than 0.1 pe. Note that minimum ionizing

particles typically produce 20-30 pe when passing through a bar. Thus the energy resolution is  $\sim 20\%$  just from Poisson fluctuations and the electronics noise does not contribute significantly.

The overall charge dynamic range requirements are set by the electronics noise level and by the need to fully measure electrical signals from the largest MPPC pulses when all 667 pixels fire.

The required timing resolution is driven by two considerations. First, a large background of neutrino interactions occur in the surrounding magnet. At full J-PARC beam power, each beam spill will result in more than 50 such interactions. Many of these interactions could cause detector activity in the FGD. Thus the FGD must have good timing resolution in order to reliably separate this activity from that initiated in the FGD scintillators. Studies showed that a timing resolution on the order of 3 ns for an FGD *vertex*, which consists of several hits, would be satisfactory. This is the most critical requirement for the timing resolution. However, better timing resolution would make it possible to distinguish track direction based on comparing hits in FGD1 versus FGD2. The goal, therefore, is to have a timing resolution of better than 3 ns for each *hit*.

Another requirement on the electronics is the time to read out the data. Although the interval between beam spills is 3 seconds, which provides more than enough time, calibration triggers, such as cosmic ray, electronic pedestal, and light pulser triggers, are taken between beam spills. Thus the maximum allowed time to read out events is set to 50 ms by the maximum data-taking rate, which is 20 Hz.

Finally, access to the electronics boards within the magnet is impossible while the experiment is running. Thus it must be possible to remotely control and monitor the condition of the boards. Furthermore, the temperature must be recorded in order to correct for temperature dependence of the photosensor response. In addition, the bias voltage of each photosensor must be set individually in order to obtain a uniform detector response. Thus, a robust slow control system is required.

## 8.2. Architecture

A brief description of the electronics arrangement was given in the Introduction (see section 1.1). Further details of its organization and operation are presented here.

The overall readout electronics system is shown in Fig. 21. As mentioned in the Introduction, the front-end electronics sits in minicrates located along the outside edges of the dark box. Each minicrate in FGD1 contains four front-end boards (FEBs) (two in FGD2) that provide the MPPCs with power and also sense and digitize the MPPC signals. A Crate Master Board (CMB) in each minicrate incorporates an FPGA to control the readout procedure. One other element in each minicrate is a Light Pulser Board (LPB) used for calibration. Each minicrate services either 240 (FGD1) or 112 (FGD2) MPPCs.

The digitized MPPC data is transferred through fiber optic links to Data Concentrator Cards (DCCs) that then transfer the data to the back-end computers for data acquisition system (DAQ) processing. The DCCs are also connected to a number of common ND280 electronics cards in order to be part of the overall ND280 triggering and clock distribution schemes. All these elements will be described in what follows.

## 8.3. Busboards and backplane

The MPPCs are mounted on busboards; each busboard holds 16 MPPCs (see Fig. 19). Sixteen LEDs are also mounted on each busboard to flash the WLS fibers near the mirrored end. The chosen LED is the LTST-T670TBKT (obtained from Lite-On Inc.) whose peak wavelength is 468 nm, well matched to the WLS fiber. It was important to ensure that each LED on a busboard would produce similar amounts of light when driven by an identical electrical pulse. Because of manufacturing differences, this uniformity could not be guaranteed without additional sorting of the LEDs. A sophisticated robotic system to sort them was therefore devised to automatically flash each LED and measure the resultant light output. Each busboard then received LEDs with similar responses. Usage of the LEDs is described in Section 8.7.

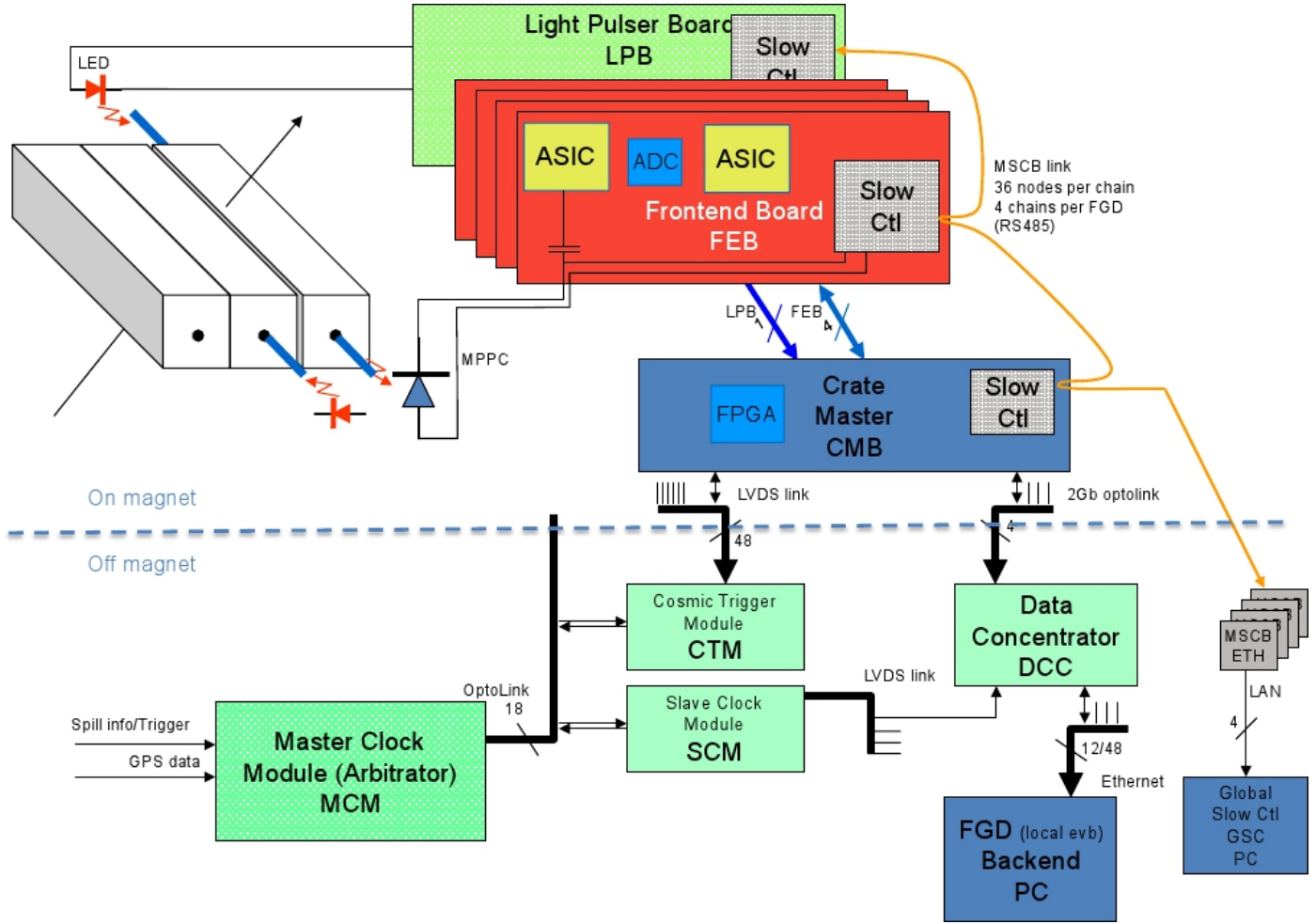


Figure 21: FGD electronics overview, showing how signals from the MPPCs are captured using the AFTER ASIC chip on the Front-End Boards; this information is then transferred through the CMBs and then off-magnet to the DCCs and the back-end computers. The upper part of this plot shows the cards that reside inside the magnet (i.e., one crate’s worth of front-end cards). The principal trigger for neutrino beam spills comes from the Master Clock Module (MCM).

The busboards are connected by ribbon cables to the electronics backplane. The backplane provides the electrical and mechanical interface between the inside of the dark box, containing the busboards and MPPCs, and the outside of the box containing the front-end electronics cards (FEBs, CMBs and LPBs). Thus besides providing common services for all the cards in the minicrate, such as power, slow control and readout, the backplanes also provide the electrical connections between the busboards and the FEBs. Care must be taken to ensure there is minimal electrical crosstalk between analog MPPC lines and that the large digital signals do not influence the small analog signals. The layout and routing of the backplane was therefore a complicated affair,

with care being taken to route the analog and digital signals on different layers of the board.

#### 8.4. Front-end electronics slow control

One critical aspect of the FGD electronics is the slow control system. *Slow Control* refers to the electronics circuitry and associated firmware located on all the front-end cards, as well as the associated software system described in Section 10. A separate slow control power source is supplied to each card, which permits continuous monitoring of the hardware without the necessity of full activation of the card. The addition of an asynchronous slow control system is also useful for providing a clean conceptual separation between elements of the electronics sys-

tem that must be recorded for each event (MPPC data, trigger types, timestamps, etc.) and elements that can be monitored less frequently (temperatures, voltages, etc.). Therefore, the inclusion of a separate slow control system makes the FGD electronics architecture more robust, since it provides an independent way of monitoring and debugging the state of the boards and simplifies the types of communication among the FEBs, CMBs, DCCs and back-end computers.

The slow control section or node on each board is operated by a microcontroller. The interface and protocol used for the communication is based on the Midas Slow Control Bus (MSCB) [22]. This bus is an RS485 multi-drop master/slave serial link. Several microcontroller families can support the MSCB protocol. The FEBs employ the C8051F133 microcontroller (obtained from Silicon Labs) with 64 kB of flash, running up to 100 MHz. The C8051F133 has internally  $8 \times 10$  bit ADCs and 32 I/O ports. Some of the I/O ports are programmed to communicate via SPI, I2C, and SST buses with other devices, enhancing the microcontroller capabilities. Each FGD has 4 MSCB chains (one per side). Each chain is composed of up to 36 MSCB nodes (6 cards/crate  $\times$  6 crates).

Each MSCB-RS485 chain is converted to Ethernet protocol in order to normalize the communication method with the rest of the ND280 apparatus. This is done by an MSCB-ETH board powered by a C8051F121 and Cypress CS9800A Ethernet chip. The data communication mechanism uses the UDP protocol.

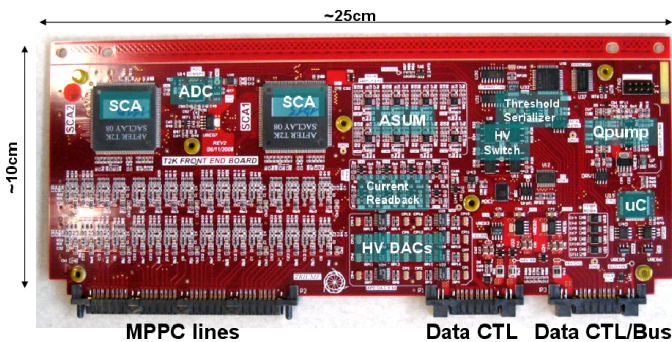


Figure 22: FGD Front-End Board with critical features indicated; its lower edge in this figure plugs into the back-plane.

As each card is described in the following subsections, the particular slow control functionality that is implemented on that card will also be described.

### 8.5. AFTER Chip and FEB

The key element of the FGD front-end electronics is the AFTER ASIC that was designed for the T2K TPC [23]. This ASIC provides a preamplifier, a shaper and a switched capacitor array (SCA) for each of 72 channels. The purpose of these elements is as follows:

- The combination of preamplifier and shaper amplifies the electrical pulse from the MPPC and also extends the pulse length. For the FGD, the AFTER ASIC preamp-shaper time constant is set to 30 ns, the lowest possible value, corresponding to a 180 ns peaking time.
- The SCA is an array of capacitors that are used to store analog samples of the shaped MPPC pulse. When the last cell in the array is reached, the ASIC will start overwriting the values in the first cell; the SCA can therefore be continuously filled until the write process is stopped by an event trigger. The sampling frequency of the SCA is tunable, but for the FGD it is set to 50 MHz. Therefore the SCA is sampled every 20 ns and the total depth of the 511-cell array is  $10.2 \mu\text{s}$ .

A critical feature of the AFTER ASIC is that the preamp-shaper combination allows sampling the waveform at a much lower frequency than would be possible if the MPPC signal was digitized directly. This strategy reduces the cost significantly while still allowing the timing resolution requirements to be met. The contents of the SCAs are digitized by a 12 bit flash ADC running at 20 MHz and the resulting data are transferred to the CMB. This process is described in section 8.6.

Fig. 22 shows the component face of a FEB. Two AFTER ASICs can be seen. Each ASIC reads out 32 MPPCs; hence one FEB reads out 64 MPPCs. Coupling an MPPC to the AFTER ASIC is not trivial, however. The dynamic range

requirement implies that two AFTER channels must be used to record both low-gain and high-gain signals from each MPPC. The signal is divided as shown in Fig. 23. Small values are used for the capacitors in the low and high attenuation branches and in the trigger branch in order to minimize the input capacitance, hence minimizing the electronics noise. Recharging the MPPC is achieved by the 100 nF capacitors. The 10 kΩ resistor in series with the 100 nF capacitor in the recovery branch means that the MPPC recovery time constant is  $667C(R/667+10\text{ k}\Omega) = 614\text{ ns}$  to first order. Here  $C = 90\text{ fF}$  ( $R = 150\text{ k}\Omega$ ) is the capacitance (resistance) of a single pixel, implying that  $667C$  is negligible compared with 100 nF. This time constant is only visible for large pulses; otherwise the pixels that do not avalanche quickly recharge the pixels that do. Fig. 23 also shows a third branch that is summed with others on the board to generate a trigger signal.

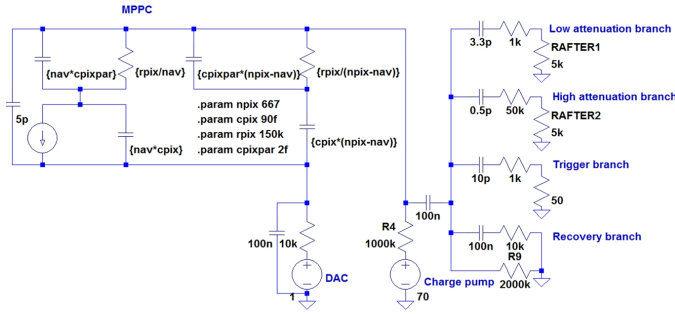


Figure 23: SPICE model of the MPPC and of the Front End Board / MPPC-AFTER coupling circuit.

Fig. 24 shows an example for the high- and low-gain waveforms for a single MPPC, for a particular event. These data are from beam tests where a pion stops in one bar and the subsequent Michel  $e^+$  is detected. The pion pulse almost saturates the high-gain channel but it is clearly resolved in the low-gain channel. The undershoot following the high-gain pulses is a consequence of the capacitive coupling on the AFTER ASIC inputs. With the MPPC operating at 0.8 V overvoltage, the high-gain channel saturates at  $\sim 80$  pixels (4096 ADC counts), while a minimum ionizing particle typically produces light activating 25-30 pixels. Thus the low-gain channel does not need to be used for minimum ionizing particles.

The rest of the FEB is used for monitoring and slow control. The slow control infrastructure is handled by the MSCB protocol that is described in section 8.4. The MPPC bias voltage is generated on-board by a charge pump circuit. Using a charge pump is necessary because only 6 V is provided to the FEB but the MPPC operating voltage is  $\sim 70\text{ V}$ . The charge pump voltage is common to all MPPCs. The individual MPPC voltages are adjusted by trimming the MPPC signal return voltage using 64 Digital to Analog Converters. Both the charge pump voltage and the trim voltage can be remotely set through MSCB. Because the MPPC gain is sensitive to the temperature (5-10 % change in pulse height per degree Celsius), each FEB also reads out eight temperature sensors mounted on its busboards close to the MPPC themselves. If the temperature variations are large, the FEB slow control system allows for adjustment of the MPPC bias voltage in order to maintain equalized MPPC gains (this feature is not presently used).

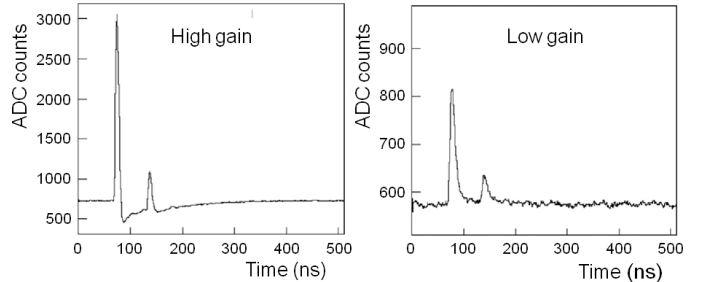


Figure 24: FGD FEB example waveform from the TRIUMF beam test showing results for the high- and low-gain channels for a single MPPC. Time is measured in 20 ns wide bins. This event can be interpreted as the particle stopping in the bar and a Michel positron subsequently emerging.

## 8.6. Crate Master Board

The Crate Master Board is the next element of the electronics; an image of a CMB is shown in Fig. 25. The core of the CMB is a Xilinx Virtex 2 Pro FPGA. The FPGA controls the record and readout phases of the AFTER ASIC, using a set of parallel LVDS clock and signal lines dedicated to each FEB. The waveform samples from each AFTER SCA are serially read out, digitized by the



ADC and stored locally on the CMB. The local storage uses a pair of Zero Bus Turnaround (ZBT) synchronous SRAMs. Stopping of data acquisition and digitization of the stored waveform happens automatically upon receipt of a trigger from the DCC. The whole process is done in  $\sim 2$  ms by simultaneously reading out the SCAs from all ASICs that are attached to the CMB (up to eight in total). This parallel readout is critical, because the analog information in the SCA cells degrades if the readout takes longer. As an added benefit, digitization is sufficiently fast that it does not significantly contribute to the overall FGD readout time.

The locally stored data can then be transferred to the Data Concentrator Cards. The connection to the DCCs is done through a full duplex RocketIO optical port running at 2 Gb/s. The DCC to CMB transfer is initiated by a packet request from the DCC (rather than by the original DCC trigger). This CMB to DCC transfer procedure will be described further in section 9.1.

In addition to the core AFTER data handling, the CMB FPGA also provides the following functionality:

- configuration of the AFTER ASIC parameters (such as the amplifier gain and the shaping time) using a serial protocol.
- processing the trigger signals from the FEBs according to programmed logic conditions.
- triggering of the LPB.

For configuration purposes, the CMB has an flash memory with a CPLD<sup>2</sup>; this allows new FPGA code to be uploaded through the optical link. The CMB FPGA firmware can therefore be upgraded and improved even after the ND280 magnet is closed. This procedure has been successfully used a number of times. As an additional safety feature, the flash memory has two banks, one of which is kept loaded with a stable version of the firmware; this ensures that the CMB can recover from upload of nonfunctional firmware.

<sup>2</sup>Complex Programmable Logic Device

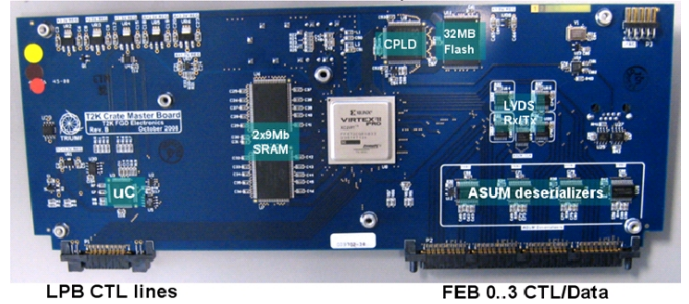


Figure 25: Crate Master Board with critical features indicated; its lower edge in this figure plugs into the backplane. The core of the CMB is the central Virtex II FPGA. The SFP (Small form-factor pluggable transceiver) fiber connector for connection to the DCC is mounted on the backside of the CMB and cannot be seen in this image.

In addition to the link to the DCC, the CMB also has a second, electrical LVDS link to the Cosmic Trigger Module (CTM); the purposes of this link will be described in more detail in section 8.10.

In order to reduce the volume of data recorded, data compression capability is programmed in the CMB. Part of this compression scheme makes use of a pulse finding/pulse height algorithm. Both of these processes are fully described in Section 9.1.

Finally, the CMB slow control microcontroller can be used to turn on/off the FPGA and to monitor the main operating voltages, currents and temperatures of the board. A separate serial link between the slow control microcontroller and the FPGA is available for transmission of particular Status/Control bits such as the geographical address of the board and the optical link state, as well as allowing for the reset of the FPGA.

### 8.7. Light Pulser Board

The Light Pulser Board is the last of the cards in each minirate. The LPB controls the pulsing of the LEDs mounted on the busboards. The purpose of the LED system is twofold:

- to test the integrity of the signal path starting from the fiber to the digitization for every MPPC channel. Light is injected near the end of the WLS fiber opposite from the MPPC and therefore can detect possible mechanical issues such as microcracks in the

fiber or problems with the fiber/MPPC coupling.

- To provide a coarse gain calibration of the MPPCs. This calibration can either be performed continuously between the beam spills or can be done in dedicated LPB runs.

There are up to 240 LEDs being driven by each LPB. Driving each of those LEDs individually is impractical. Therefore, sets of four LEDs on each busboard are ganged together and driven by a single LPB pulser. Hence there are 60 independent pulsers on the LPB.

Triggering the LED pulses is controlled by the CMB. Specifically, if the CMB receives a ‘LED-type’ trigger then it will send a signal to the LPB to fire the LEDs. The CMB will then wait for a couple of microseconds before initiating readout of the AFTER ASICs. This will ensure that the LED pulses actually occur near the middle of the AFTER waveforms.

Like the FEB and CMB, the LPB has a slow control microcontroller to monitor board functions. In addition to monitoring voltages and temperature, the LPB slow control also allows the user to specify the intensity of the LED pulse by setting a DAC level for each group of four pulsers (i.e. a separate DAC is used for each busboard).

### 8.8. Infrastructure

The front-end electronics require a number of different voltage levels for the various cards. Specifically, +6 V digital, +6 V analog, +4 V and -6 V voltages are supplied to the cards using a pair of Wiener PL508 power supplies. The slow control on the front-end cards is powered separately using a +5 V level from a Xantrex power supply. The Wiener power supplies are hardware-interlocked to the Xantrex power supply; if the Xantrex supply drops below 4.5 V the Wieners will automatically shut off. This ensures that the cards will not be fully powered without slow control monitoring.

The total power consumed by the front-end electronics is approximately 1500 W; this heat is extracted from inside the magnet by the cooling system described in section 7.4.

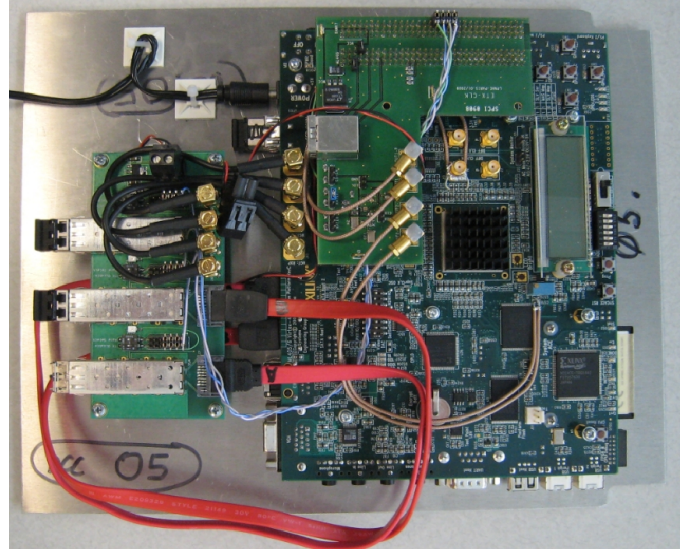


Figure 26: FGD Data Concentrator Card assembly; ML405 with extension cards mounted on support.

### 8.9. Data Concentrator Card

Each of the 48 CMBs has an optical link connected to a Data Concentrator Card. The DCCs start and stop the data acquisition process on the front-end electronics; also, after the front-end acquisition has finished, the DCCs request channel data packets from the CMBs and format the data packet before sending it to the DAQ over ethernet. Each DCC is presently composed of an ML405 evaluation board and 2 custom cards. Each DCC possesses four RocketIO optical links and can read out data from four CMBs. Twelve DCCs are therefore needed to read out the full FGD.

Each ML405 board is based on a Xilinx-IV FPGA with a PPC405/300MHz microprocessor and Gigabit Ethernet port. The DCC functions are implemented as FPGA firmware and microprocessor tasks. The FPGA part of the DCC has custom VHDL firmware that interfaces with the RocketIO ports and provides the synchronous trigger distribution. The DCC microprocessor has been configured to run a simple Linux kernel (2.6.23-rc2) using the BusyBox utility package. This Linux kernel hosts a reduced Midas Data Acquisition front end directly on the DCC; more details can be found in section 9.2.

The DCC assembly is shown in Figure 26. There are two custom extension boards added

to the ML405. The first board provides a 4-to-1 SMA/RocketIO Optical link converter and 3 SATA/RocketIO to 2 Optical link converters. The second board provides the interface to the trigger module and also provides the global 200 MHz clock for RocketIO operation.

### 8.10. Interface to ND280 electronics

There are a number of elements of the FGD electronics that must interface with the global ND280 electronics system. Many of these elements can be seen schematically in Fig. 21. They are:

- MCM/SCM Trigger Reception: events in ND280 are triggered by either the Master Clock Module (MCM) if in global mode or by the FGD Slave Clock Module (SCM) if in local mode. In either case, the triggers are passed through the FGD SCM which distributes an LVDS signal over Cat.-6e cables to the twelve DCCs. These triggers are then passed on to the CMBs over the RocketIO optical link and initiate the AFTER ASIC readout procedure that was described in the section 8.6.
- Global Clock: the FGD SCM also provides a 100 MHz clock to the DCCs, which is in turn passed on to the CMBs. The FGD SCM is phase-locked to the MCM 100 MHz clock; the FGD electronics is therefore phase-locked to the other ND280 subdetectors, thereby simplifying cross-detector time calibration.
- FGD Cosmic Trigger: the FEBs have dedicated Analog Sum (ASUM) circuitry capable of generating a local trigger. Each FEB sends 8 separate ASUM triggers to the CMB, which then makes a decision whether or not the crate has satisfied its trigger logic conditions. If so, a trigger is sent over a Cat.-6e LVDS link to the FGD Cosmic Trigger Module. If the triggers from the CMBs satisfy the overall CTM trigger condition (which usually requires that at least two CMBs in each FGD have fired), then a global ND280 trigger can be generated. This trigger can select cosmic

rays that pass through both FGDs, which is a useful tool for calibration.

- FGD Timing Marker: the CTM provides to each CMB an LVDS timing marker pulse, which is injected asynchronously into spare channels on the AFTER ASICs. Since the timing marker pulses are injected into all FEBs at the same time (modulo cable length differences), the recorded timing markers can be used to correct for clock phase differences and digital jitter.

## 9. Data acquisition and compression

The Data Acquisition System (DAQ) is responsible for transferring the digitized MPPC waveform from the CMB RAM to the DCC and from the DCC to the back-end computers. The DAQ therefore consists of a combination of FPGA firmware on the CMBs and DCCs, as well as software on the DCCs and back-end computers. One of the major challenges for the DAQ is to reduce the volume of data written to disk. If the full uncompressed FGD data for every event were saved, the maximum recorded event rate would be  $\sim 2.5$  Hz, with a data rate of  $\sim 60$  MByte/s (limited by the CMB to DCC bandwidth). However, the DAQ is required to record events at a trigger rate greater than 20 Hz with a data rate of a MByte/s for the FGD. Clearly the DAQ must therefore provide a significant amount of data compression while maintaining a high trigger rate.

A typical particle interaction will deposit charge in only approximately 60 of the 8448 scintillator bars; this means that all relevant information about a particular event can be collected from only a small fraction of the detector. In addition, MPPC dark noise pulses must also be saved for calibration purposes; however, not all the waveform information for noise hits must be saved. These two facts suggest that considerable data reduction is possible.

### 9.1. CMB online data compression

The choice was made to implement data compression using VHDL firmware on the CMB

FPGA [24]. The advantage of implementing the data compression at the CMB level is that it allows the process to be highly parallelized. It would have probably been impossible to provide the same degree of compression if it had been done at the DCC or back-end computer level. The following explains how this CMB compression is implemented.

The custom DCC to CMB data transfer protocol starts when the DCC requests from the CMB a data packet from a list of channels that the DCC specifies. The CMB processes the list of channels until it finds a pulse to process and transmit in a data packet, or reaches the end of the list. The small size of the compressed data packets allows the DCC to read out all four CMBs in parallel. This transfer protocol is efficient only when a large fraction of the FGD channels are completely zero-suppressed because the number of DCC data requests and CMB transaction overhead is reduced; the efficiency of the transfer protocol is therefore dependent on effective data compression.

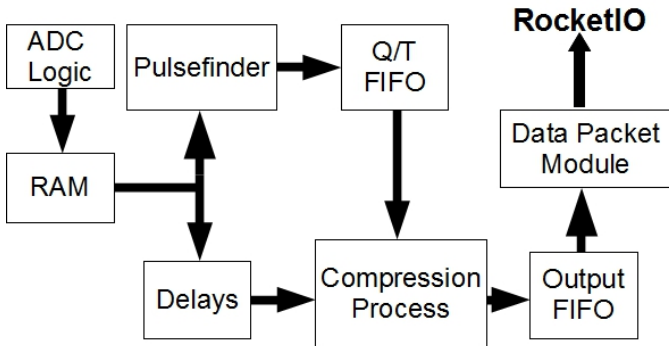


Figure 27: FGD channel readout and data compression processes implemented in CMB firmware.

There are two elements to the data compression: the ability to quickly and efficiently identify pulses (pulse finding) and the compression of the information from that pulse. The procedure is shown schematically in Fig. 27. The pulse finder algorithm is a local peak detector that compares the sum of amplitudes during consecutive rising and falling edges to a threshold to identify a pulse. The current system uses a threshold of 30 ADC counts, roughly equivalent to peak pulse heights of 15 ADC counts. This provides

greater than 98 % pulse finding efficiency for pulse heights above 20 ADC counts (assuming nonoverlapping pulses). This threshold is well below the single-pixel pulse height distribution (with mean pulse height measured at  $\sim 40$  ADC counts and  $\sigma \sim 6$  ADC counts), but is large enough to suppress most baseline fluctuations (with mean  $\sigma$  of 3 ADC counts). The pulse-finding efficiency increases with larger pulse height with an efficiency of effectively 100 % for large pulses from minimum ionizing particles.

Pulse height is measured as the difference between the pulse peak height and a sample measured a fixed time before the peak to estimate the channel baseline. The approximately constant gain across all MPPCs established by overvoltage tuning allows the same threshold to be used for the entire system. ADC samples are read from the RAM and processed by the firmware-based pulse finder. When a pulse is identified, the pulse finder writes the pulse height and time information into the Q/T FIFO (Q/T = charge/time). The Q/T FIFO feeds a separate compression process to zero-suppress a delayed sequence of ADC samples. The amount of delay depends on the desired number of samples in the data packet prior to the pulse rising edge, as well as the time required for the pulse finder to identify a pulse and calculate its height.

Additional data reduction decisions are made by the compression process based on the identified pulse height. Specifically, a decision must be made whether to save only the pulse height and time for a pulse or whether to also save the ADC samples around the peak position. Saving the ADC samples is critical for calculating a precise time for the pulse during offline data processing. But having a precise time is only important for pulses associated with physics hits; it is not important for dark noise pulses. The pulse height spectrum obtained from cosmic-ray trigger data (see Fig. 28) shows that the dark noise pulses dominate the spectrum for pulse heights below 200 ADC counts, while larger pulses are primarily produced by cosmic muons interacting in the scintillator bars. Therefore, ADC samples for a pulse are saved only if the pulse height is greater

than the dark noise threshold, which is 200 ADC counts.

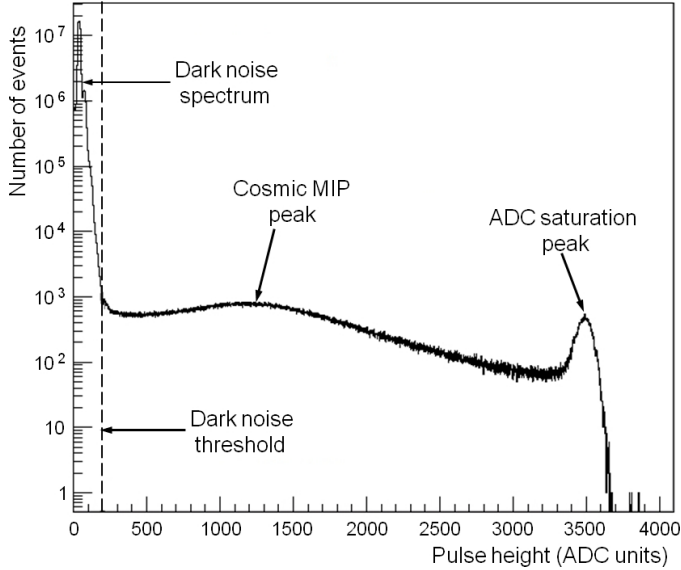


Figure 28: MPPC pulse height distribution for cosmic trigger events, with dark noise threshold displayed.

In fact, even discarding ADC samples for dark noise pulses does not provide a sufficient degree of data compression. The total average data size for dark noise pulse information processed using this scheme is  $\sim 280$  kB per event, compared with  $\sim 20$  kB for pulses due to particle interactions. Dark noise information can be discarded or retained on an event-by-event basis since it is necessary only for long-term calibration; therefore the total data rate can be adjusted by discarding dark noise pulses for some fraction of the events. In the current implementation, the dark noise data are typically saved only 10 % of the time.<sup>3</sup>

After all the samples for each channel are read from RAM, the contents of the output FIFO are moved into the RocketIO clock domain of the CMB and used to form the data packet that is sent over the optical link to the DCC.

## 9.2. Midas Data Acquisition System

The FGD (like the rest of ND280) uses the MIDAS system [25] as the basis for the DAQ. The

<sup>3</sup>An alternative method is to always retain the dark noise data in the CMB but discard it in a back-end process after updating an online charge histogram. This scheme will be implemented in the future.

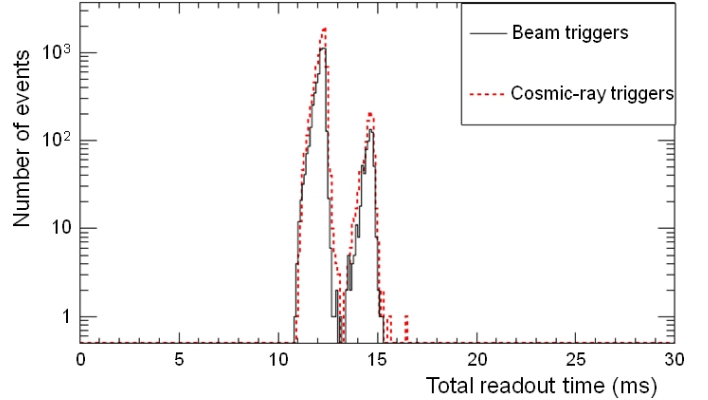


Figure 29: Total time to read out FGD, for both beam and cosmic-ray events. These measurements are provided by the FGD SCM. The two distinct peaks correspond to events where we read out all dark noise pulses (right peak) and where we completely suppress the dark noise pulses (left peak).

core of the FGD DAQ system is a set of Midas front-end programs that run on each of twelve DCCs; as mentioned above, running Midas programs directly on the DCCs is possible because of the Linux kernel running on the DCCs. This DCC program initiates the CMB to DCC transfer that was described in the previous section; the programs also handle the transfer of data from the DCC to the back-end FGD computer.

One complication of the FGD DAQ is that it is necessary to be able to run in both a local FGD-only mode, as well as in a global mode with all the rest of the ND280 detectors. A cascade system has been designed to provide this functionality. The first level of the cascade is the FGD DAQ that runs on the FGD back-end computer. In FGD-only local mode the data is stored only on a disk on the FGD DAQ. In the global ND280 mode [26], the FGD data is transferred to a different global DAQ computer where it is merged with data from other subdetectors before being saved to disk.

All of the processing and transfers by the FGD DAQ must be completed within a time period that is compatible with the overall ND280 DAQ. Fig. 29 shows FGD SCM measurements of the total time between the reception of the trigger to the time at which the busy signal was disabled by the FGD DAQ software. As can be seen, the time to read out the FGD is always less than 20 ms.

Thus in normal experimental conditions the FGD can run at a 50 Hz trigger rate, comfortably exceeding the 20 Hz requirement.

## 10. Slow Controls and monitoring of FGD components

As described in section 8, several of the FGD components communicate with a PC for control functions and monitoring. All of these functions are performed by front-end tasks connected to one instance of the MIDAS framework system [22]. This system is similar to the DAQ system and is common to all ND280 detectors. The MIDAS framework provides templates for front-end tasks as well as drivers for the various means of connecting to the hardware.

The slow control front-end tasks for the FGDs are:

- front-end electronic boards (FEB, CMB, LPB) control and monitoring: connected via MSCB
- Wiener power supplies (3) control and monitoring: connected via Ethernet
- Xantrex power supplies (2) monitoring: connected via MSCB providing power to slow control section of front-end electronic boards and DCC
- DCC power control module: connected via MSCB
- target water system monitoring: connected via MODBUS
- target water temperature sensor monitoring: connected via MSCB
- FGD SCM and CTM temperature sensor monitoring: connected via MSCB

Each of the front-end tasks connects to a common MIDAS online database (ODB) where all settings and sensed values are stored. Users communicate with the ODB via web pages. The MIDAS framework provides generic web pages for display of settings and sensed variables but custom web

pages have been written to facilitate user interaction for control of power supplies and for the FGD electronics front-end boards.

The most extensive front-end program controls and reads back the bias voltage for each MPPC as well as temperatures on the busboards and on each electronic board, and a few humidity sensors. Power to the main section of the boards is also controlled through this program. Eight instances run in parallel connecting to the eight MSCB communication chains (see section 8.4)

The MIDAS task MLOGGER logs all sensed values stored in the ODB at fixed intervals defined by the user for each type of variable. The usual frequency is 5 minutes but faster frequencies were used when debugging or watching a critical front-end component. For example a frequency of 10 seconds was used to troubleshoot problems with the FGD water target water system. The FGD electronics front end is a special case where the sensed values are stored at a fixed interval of 5 minutes or when the user modifies electronics settings such as the bias voltages.

These variables are logged in a MySQL “Slow Control Database” by MLOGGER, which creates tables automatically, based on the labels of the variables in the ODB. There are 420 tables populated with FGD slow control variables. The MIDAS web server provides a versatile mechanism to define history plots of any of these variables, which the user can consult for any given period or see the plots grow in real time.

## 11. Calibration

The calibration involves two almost independent tasks: charge (Sec. 11.1) and time (Sec. 11.2) calibration. The procedures described in this paper are those currently used to produce physics results. (Further improvements are expected to be implemented in the future.)

### 11.1. Charge calibration

The purpose of the charge calibration chain is to convert a raw pulse height ( $PH$ ), measured in ADC channels from a digitized MPPC waveform, to a normalized value representing the en-

ergy deposited in a scintillator bar. This normalized value should be insensitive to any changes in operating conditions encountered during the course of a data-taking run.

### 11.1.1. Electronic high-/low-gain calibration

The low-gain channel extends the dynamic range to include energy depositions yielding more than about 90 avalanches, which saturate the 12-bit ADC on the high-gain channel. The signal-to-noise ratio in the low-gain channel is too small to allow efficient detection of single-pixel avalanches, but becomes good above 10-pixel avalanches. If the high-gain pulse corresponds to more than about 65 avalanches, then the waveform from the low-gain channel is used. The relationship between the responses of corresponding high and low-gain channels is linear, characterized by the constant

$$C_{HL} \equiv \frac{PH_H}{PH_L}. \quad (2)$$

Here  $PH_{H[L]}$  denotes the pulse height measured in the high-(low-)gain channel. The value of  $C_{HL}$  is measured for each MPPC using cosmic rays that deposit energy in the bars creating avalanches in more than 10 pixels while encompassing the full range of energies measurable by the high-gain channel. The value of  $C_{HL}$  averaged over all the MPPCs is 8.81, with an RMS spread of 0.27.

### 11.1.2. Normalization by temperature-dependent single-avalanche gain

The next step in the calibration chain is to calculate the number  $N_{av}$  of pixels avalanching by normalizing the measured pulse height  $PH$  by the average pulse height  $\langle PH_1 \rangle$  corresponding to a single-pixel avalanche:

$$N_{av} = PH / \langle PH_1 \rangle \quad (3)$$

The distribution of dark noise pulse heights is used to measure  $\langle PH_1 \rangle$  for each MPPC. The first peak of the distribution is fitted by a truncated Gaussian,  $\langle PH_1 \rangle$  being the location of this peak. A typical example is shown in Fig. 30. Dark noise spectra are accumulated in dedicated runs taken with periodic triggers. Such spectra are also

obtained during physics data-taking, since dark noise pulses are present in the 10  $\mu$ s time windows during which MPPC waveforms are digitized.

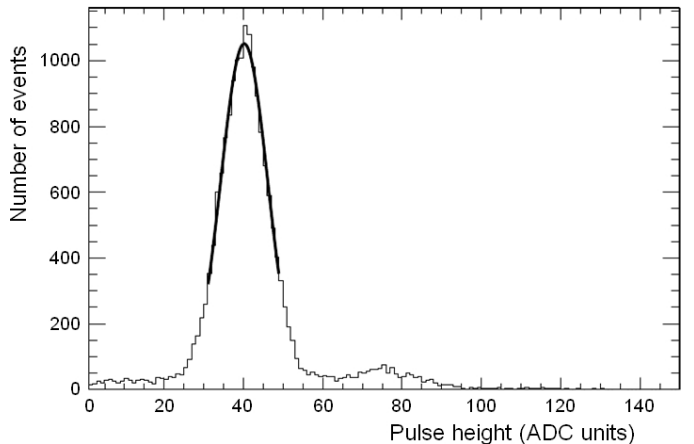


Figure 30: Typical dark noise pulse height distribution, showing the truncated Gaussian fit.

The single-avalanche pulse height  $\langle PH_1 \rangle$  scales with the MPPC gain, which is proportional to the overvoltage, the difference between the operating and breakdown voltages. The breakdown voltage depends on temperature [27], which can change during running. The operating voltage is kept constant in normal operation, but the temperature varies, by at most  $\pm 2^\circ C$ . The change in gain is expected to be less than 10 %, which does not justify developing a feedback system to adjust the operating voltage while the experiment is running. Instead it is compensated in the analysis.

Rather than analyzing dark-noise spectra to extract  $\langle PH_1 \rangle$  often enough to track possible temperature changes, it is more convenient and adequately accurate to correct for the temperature changes by applying a correction based on the temperature measured in the vicinity of each MPPC. At a fixed temperature,  $\langle PH_1 \rangle$  is expected to vary linearly with operating voltage, if the pixel capacitance were independent of voltage. However, it was empirically determined that a quadratic dependence provided a better description of the measured variation (see Fig. 31), in agreement with [28]. For each MPPC,  $\langle PH_1 \rangle$  is calculated using the relation

$$V - C_T(T - T_0) = V_{bd,0} + (1/G)\langle PH_1 \rangle + C_G\langle PH_1 \rangle^2 \quad (4)$$

where  $V$  and  $T$  are the operating voltage and temperature at the time of measurement,  $V_{bd,0}$  is an estimate of the breakdown voltage at  $T_0$ ,  $G$  is an empirically determined parameter in units of ADC counts/V, which can be interpreted as the product of the electronic gain with the capacitance of the MPPC in parallel with that of its busboard trace, and  $C_G$  an empirical parameter accounting for the quadratic dependence. This quadratic term receives contributions from both the slight nonlinearity of the intrinsic dependence of the MPPC gain on overvoltage as well as the effect of a large resistor in series with the MPPC bias voltage source in combination with the dependence of the MPPC dark noise rate on overvoltage. The parameter  $C_T$  is a constant with an empirically determined value of  $57 \pm 3$  mV/deg, in agreement with expectations [27] from lab bench tests. The parameters  $V_{bd,0}$ ,  $G$  and  $C_G$  are determined separately for each MPPC from a series of dark-noise spectra acquired at various voltage settings. Each such “voltage scan” is done in a time sufficiently short to ensure that the temperature did not vary significantly from  $T_0$ . During the subsequent analysis of data, periodic extraction of  $\langle PH_1 \rangle$  from a dark noise spectrum at the temperature of that time is used to confirm that Eq. 4 is producing an appropriate estimate. It is found that values of  $\langle PH_1 \rangle$  extracted from dark noise spectra and those estimated using Eq. 4 agreed to better than 2 % during the entire first year of running.

Each MPPC temperature is estimated as the average value from eight sensors located on the MPPC busboards in that region of the FGD. The temperature and operating voltage values are recorded every few minutes and logged in the slow control database. The constants  $V_{bd,0}$ ,  $G$ , and  $C_G$  are stored for each MPPC in the calibration database.

Values of breakdown voltage determined from fits to voltage scan measurements match well with the appropriately scaled recommended operating voltages for individual MPPCs as provided by the manufacturer.

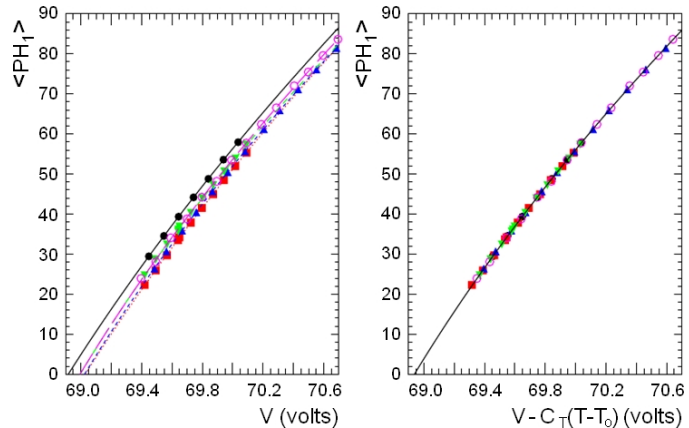


Figure 31: Pulse height  $\langle PH_1 \rangle$ , measured in ADC counts, for single-pixel avalanches vs applied voltage for a typical MPPC, measured at various temperatures. The plot on the left is without temperature correction; the points on the right plot have been temperature corrected.

### 11.1.3. Effects on $N_{av}$ of variations in overvoltage

The number  $N_{av}$  of pixels avalanching for a given number of photons hitting the MPPC depends on the photodetection efficiency, and the cross talk and after-pulsing probabilities. Temperature variations change the MPPC breakdown voltage and hence overvoltage, the difference between the operating and breakdown voltages. This affects not only the MPPC gain but also the above three attributes, as well as the dark noise rate [28]. The variation of  $N_{av}$  with temperature for a constant light pulse intensity must be compensated.

The variation of  $N_{av}$  with overvoltage was studied using an electron beam during the M11 beam tests at TRIUMF (see Sec. 12), and with self-triggered high-energy cosmic rays *in situ* at J-PARC. The operating voltage was intentionally varied while keeping the beam or cosmic trigger condition constant, and the data were taken while the temperature was not changing significantly. Events were selected to define a reproducible narrow distribution in energy deposition in each bar, from either passing electrons or muons. At each operating voltage setting, the mean pulse height  $\langle PH \rangle$  from this distribution was measured, as well as  $\langle PH_1 \rangle$  from dark noise. Over a limited range of overvoltage, the data can be fit by this empirical



relation:

$$\langle N_{av} \rangle \equiv \frac{\langle PH \rangle}{\langle PH_1 \rangle} \propto C_o + C_\epsilon \langle PH_1 \rangle \quad (5)$$

Such a relationship would be expected for such a fixed (small) light-pulse intensity if both the photodetection efficiency  $\epsilon$  and MPPC gain increased linearly with overvoltage. Lab bench tests demonstrated such a linear behavior of the gain, and an approximate such behavior of  $\epsilon$  over a limited range [28]. The values of the constants  $C_o$  and  $C_\epsilon$  were found to be  $-0.0885 \pm 0.0071$  and  $0.0338 \pm 0.0007$  ADC counts<sup>-1</sup>, respectively, where their normalization was chosen so that the factor  $C_o + C_\epsilon \langle PH_1 \rangle$  is unity for the average value of  $\langle PH_1 \rangle$  across all the MPPCs. It was found that only one set of values was required for all MPPCs.

Over a wider range of overvoltage  $\Delta V$ , departures from Eq. 5 can be expected. The lab bench tests in [28] measured not only the dependencies of the gain and photodetection efficiency  $\epsilon$ , but also the number  $n_{sec}$  of secondary avalanches (cross talk plus after-pulses) per primary avalanche. The behavior of  $\epsilon$  is consistent with the expected shape [29] for saturation of its only overvoltage dependent factor, the Geiger efficiency  $\epsilon_{Geiger}$  (the probability for a photoelectron to cause an avalanche), while  $n_{sec}$  was found to vary quadratically with  $\Delta V$  for  $\Delta V < 1.5V$ .<sup>4</sup> Hence a more general functional form might be employed for the relevant product  $\epsilon(1 + n_{sec})$  expressed directly in terms of  $\Delta V = V - C_T(T - T_0)$  (see Eq. 4). Nevertheless, Eq. 5 is used in the calibration chain because it is a simple parameterization that matches the data well enough over the temperature range experienced. Thus a temperature-corrected value of  $N_{av}$  is computed:

$$N_{av,cor} = \frac{N_{av}}{C_o + C_\epsilon \langle PH_{1,proxy} \rangle}. \quad (6)$$

<sup>4</sup>The lab bench test data of Ref. [28] indicate that these two sources of nonlinearity cause opposite curvatures in the plot of  $\langle PH \rangle$  versus  $\langle PH_1 \rangle$ , with that of secondary avalanches expected to dominate. On the other hand, the data from the M11 test beam studies suggest a curvature opposite to that expected from this dominance. This inconsistency is presently not understood.

Here  $\langle PH_{1,proxy} \rangle$  serves as a proxy for  $\Delta V$  through the intrinsic properties of the MPPC, so the value used here for each MPPC is its value for  $\langle PH_1 \rangle$  corrected for the effects of the capacitance of its busboard trace, the length of which varies among those on each busboard.

#### 11.1.4. Saturation of the MPPC pixel population

Since each MPPC has a finite number of pixels, it is expected that measured pulse heights will saturate with increasing light levels, as each pixel may be hit by multiple photons and the fraction of pixels avalanching begins to become of order unity. (This is why the discussion in the preceding subsections was limited to small light-pulse intensities.) For the case of a uniform distribution of the photons hitting the entire MPPC and assuming infinite recovery time (i.e., a pixel cannot avalanche multiple times within the electronic pulse shaping time), an analytic formula for the saturation can be derived:

$$\langle N_{av,cor} \rangle = N_{pix} (1 - e^{-\epsilon(1+n_{sec})\langle N_{ph} \rangle / N_{pix}}). \quad (7)$$

Here  $\langle N_{ph} \rangle$  is the mean number of photons hitting the MPPC,  $\epsilon$  is its photodetection efficiency,  $n_{sec}$  is the number of cross talk or after-pulse pixels fired per primary avalanche, and  $N_{pix}$  is the number of pixels in the device. Bench tests using a nonuniform photon distribution from a wavelength-shifting fiber have shown that this formula adequately models the FGD MPPCs' response when the number of avalanches is less than 300, provided that  $N_{pix}$  is replaced by a smaller effective value  $N_{pix,eff}$ . In these studies [30], a 405 nm laser was used to excite the Y11 fiber. The green light reemitted by the Y11 fiber was detected by an MPPC using the FGD electronics system. No blue light from the laser could reach the MPPC directly. At a low light level where there was a substantial probability  $p_0$  of the MPPC producing no response from the light pulse, this probability was measured and Poisson statistics was assumed to calculate  $\epsilon \langle N_{ph,1} \rangle = -\ln(p_0)$ . (Note that this normalization point does not involve secondary avalanches.) Scaling from this value of  $N_{ph,1}$  at low light level, the amount of light  $N_{ph}$  hitting the MPPC was

tuned using digital variable attenuators and monitored using a PIN diode. The parameters that best fit Eq. 7 to the dependence of  $N_{av}$  on  $\epsilon\langle N_{ph}\rangle$  measured at the nominal operating voltage are  $N_{pix,eff} = 476$  and  $n_{sec} = 0.03$  [30]. This fit is over the range  $0 < N_{av} < 450$ , and there agrees with the data within 10 %, as shown in Fig. 32. The fit diverges from the data for larger light levels, which are rarely encountered in normal FGD operation. The parameter  $N_{pix,eff}$  is smaller than  $N_{pix} = 667$ , the total number of physical pixels in the MPPCs, because the fiber does not in fact uniformly illuminate the MPPC’s active area. For the largest light levels, the data exceeds the number of physical pixels. This is possible because a pixel is able to quickly recharge by drawing charge from other pixels in the same device, and re-fire within the light decay time constant of the fiber, which is about 7 ns.

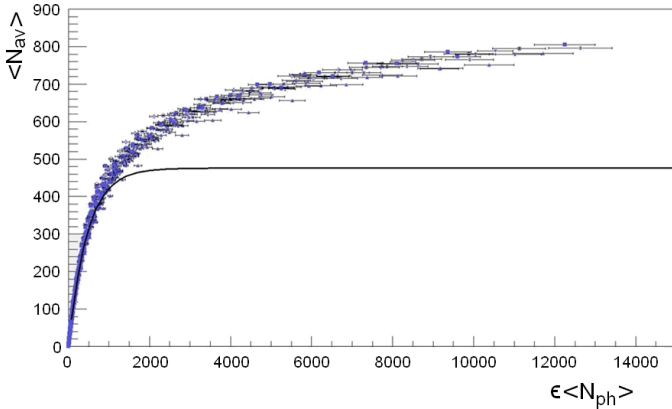


Figure 32: Measured response of an MPPC in terms of the number  $N_{av}$  of avalanching pixels, when illuminated by light from several different wavelength-shifting fibers, as a function of  $\epsilon\langle N_{ph}\rangle$ . The experimental conditions and fitted curve are described in the text.

In the present analysis of FGD data, the number  $N_{DPE} \equiv \epsilon(1 + n_{sec})N_{ph}$  of “detectable<sup>5</sup> photoelectrons” (primary plus secondary) is calculated from  $N_{av,cor}$  of Eq. 6 by inverting Eq. 7, using the values  $N_{pix,eff} = 396$  for all MPPCs. The light injection system is expected to eventually provide individual values of these constants for each MPPC.

<sup>5</sup>The quantity  $N_{DPE}$  differs from the number of photoelectrons by the factor  $\epsilon_{Geiger}$ .

#### 11.1.5. Correction for bar-to-bar variations

Given enough data, it becomes possible to check whether the number of photons hitting each MPPC not only remains constant for a constant energy deposit in that FGD scintillator bar, but also is the same for all bars. There are a number of reasons why small differences might be expected. These include minor variations in the fiber/MPPC coupling, variations in scintillator material, variations in fiber mirroring, variations in the diameter of the hole in the bars and the exact position of the fiber within the hole, etc. It was determined that such variations could be accounted for by introducing an additional correction constant  $C_{bar}$  for each bar, representing the factor by which the efficiency for conversion of energy deposition in the bar to  $N_{ph}$  photons hitting the MPPC differs from its value averaged over the whole FGD.

The values of  $C_{bar}$  were determined from cosmic ray data by using tracking information to compute the track length  $\Delta l$  through each bar, and then by comparing the distributions of  $N_{DPE}/\Delta l$  for all bars. Consistent results were obtained from two separate, similar, but independent, data sets. The spread of values of  $C_{bar}$  is about 7 %, as illustrated in Fig. 33. The values are stored in the Calibration Database for use in analysis.

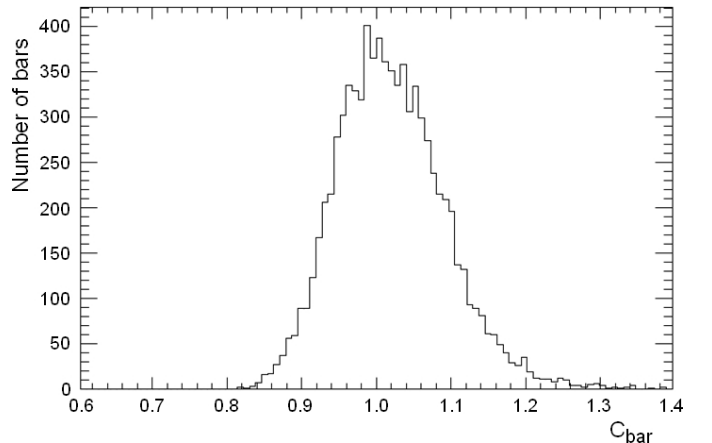


Figure 33: Distribution of the bar-to-bar correction constant  $C_{bar}$  for all FGD MPPC’s for several “voltage scans”.

#### 11.1.6. Correction for light loss along the bar

The light attenuation in each wavelength-shifting fiber was measured on a test bed, as re-

ported in Sec. 4. However, the correction of the FGD data for the dependence of the MPPC response on the position along the scintillator bar of the passing particle track is based on *in situ* measurements of cosmic rays using tracking information to identify this intersection point.

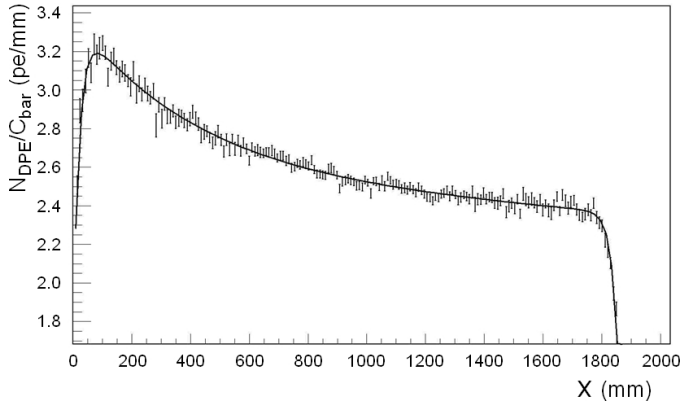


Figure 34: Number  $N_{DPE}/C_{bar}$  of intercalibrated detectable photoelectrons for cosmic ray events, as a function of hit position along the length of the bar. The data are compared to the empirical fit given in Eq. 8.

Fig. 34 shows the measured yield  $N_{DPE}$  of detectable photoelectrons from cosmic ray events as a function of the distance of the hit from the MPPC. The light yield is highest nearest the MPPC, dropping by  $\sim 25\%$  at the far end. The overall shape of the attenuation curve is consistent with that measured during the fiber testing (see Section 4), except near either end of the bar. For hits occurring within  $\sim 5$  cm of the end of the bar there is a deficit in light yield that is due to light leaking out the uncovered end of the bar before it is all absorbed in the wavelength shifting fiber. Empirically the light yield as a function of hit distance from the MPPC is well-described by:

$$I(x) = I_0 \left( 1 - \frac{1}{2}e^{-x/M} - \frac{1}{2}e^{-(D-x)/M} \right) \times \left( e^{-(x+A)/S} + Be^{-(x+A)/L} \right) \quad (8)$$

where  $I_0$  is a normalization constant,  $x$  is the distance of the hit from the end of the bar closest to the MPPC,  $D = 1864.3$  mm is the length of the bar,  $A = 41.0$  mm is the extra length of fiber extending beyond the end of the bar between the

MPPC and the bar's end,  $S = 410 \pm 60$  mm and  $L = 23600 \pm 2900$  mm are the short and long attenuation lengths, and  $B = 0.739 \pm 0.005$  is the relative normalization between the long and short components of the fiber's attenuation curve. The factor in the first set of parentheses represents an exponential decrease in light yield very close to the ends of the bars with length scale  $M = 21.55 \pm 0.28$  mm, while the second factor is the overall attenuation from the fiber itself.

Eq. 8 is used together with the factor  $C_{bar}$  defined in Sec. 11.1.5 to correct the quantity  $N_{DPE}$  defined in Sec. 11.1.4, which is proportional to the number  $N_{ph}$  of photons incident on the MPPC, to yield a quantity that is assumed to be proportional to the number  $N_{scint}$  of photons produced in the scintillator.

#### 11.1.7. Scintillation photons to energy

The calibration steps described in the previous subsections correct the MPPC response for its temperature dependence, differences among bars, and the location of the energy deposition along the bar. The resulting corrected response is assumed to be proportional to the number  $N_{scint}$  of scintillation photons. The conversion of this response to energy deposition in the scintillator requires not only an empirically determined normalization constant (about 21 detectable photoelectrons per MeV), but also consideration of non-linearity in the scintillator response. It is well known that when charged particles lose energy by ionization in a scintillator (especially a plastic scintillator), the light yield at high ionization density is quenched below the linear extrapolation from low ionization density. The scintillator response is well represented by Birks' formula [31]:

$$\frac{dN_{scint}/dx}{C_{scint} dE/dx} = \frac{1}{1 + C_B dE/dx}. \quad (9)$$

Birk's constant  $C_B$  was measured by the SCIBAR Collaboration [32] for protons incident on extruded scintillator composed of the same material as the FGD bars. For this analysis, we adopt their value ( $C_B = 0.0208 \pm 0.0003(\text{stat}) \pm 0.0023(\text{sys})$  cm/MeV).

The final normalization factor required to convert the resulting corrected response to energy deposition incorporates the product  $\epsilon(1 + n_{sec})C_{scint}$  as well as the efficiencies for optical coupling of the scintillator to the fiber and thence to the MPPC. This factor is empirically determined as that required to produce a measured distribution of energy depositions by cosmic rays that matches that predicted by a detailed simulation accounting for the kinematic distribution of the cosmic ray flux, as well as the dependence of the FGD trigger efficiency on the cosmic ray track properties. Great care was taken to ensure that the simulated spatial and angular distributions of the cosmic ray tracks reproduce the data. Section 13.3 provides more information about this simulation. Note that since the deposited energy depends on the path length through the scintillator, measured energy depositions can be compared to expectations only for hits belonging to accurately reconstructed tracks that define the path length for each hit.

Figures 45 and 46 show energy deposition by particles stopping in an FGD, reconstructed from experimental data recorded with the neutrino beam and a cosmic ray trigger, respectively. The agreement of the distributions with the curves representing simulated energy deposition for the same particle ranges demonstrates that the calibration chain operates correctly.

### 11.2. FGD timing calibration

The FGD time calibration involves the following elements:

- Pulse fitting.
- FGD internal time calibration using timing markers.
- FGD internal time calibration using FEB-to-FEB corrections.
- Corrections to align FGD times with other subdetectors (not described in this paper).
- Calculation of average time for tracks in each FGD using timing for each hit, including light travel time correction.

#### 11.2.1. Pulse fitting

Recorded waveforms are fitted in order to determine the hit time as accurately as possible. In order to save computation time, only waveforms with pulse heights larger than 150 ADC counts ( $\sim 4$  avalanches) are fit. The functional form of the fitted pulse is:

$$y(t > t_0) = B + A \left( \frac{t - t_0}{\tau} \right)^4 \left( 1 - \frac{t - t_0}{\lambda\tau} \right) \times e^{-\frac{t-t_0}{\tau}}, \quad (10)$$

with  $B$  the waveform baseline,  $A$  the pulse amplitude,  $t_0$  the start time of the pulse,  $\tau$  the amplifier-shaper time constant and  $\lambda$  the time constant of the undershoot following the pulse. Only the parameters  $A$ ,  $B$  and  $t_0$  are allowed to float in the fit; the parameters  $\tau$  and  $\lambda$  are fixed to 43.4 ns and 6.93, respectively. Only the leading edge of the FGD pulse is fit; specifically, the fit is over the region from 240 ns before the actual peak ADC sample up to the peak. Fitting the leading edge was found to provide optimum timing resolution by minimizing the sensitivity of the measure to after-pulsing and late photons (typically reflected from the mirrored end). The fitted time  $t_0$  is stored and processed by the subsequent time calibration steps. If the high-gain pulse corresponds to more than about 65 avalanches, then the fitted time from the low gain channel is used.

#### 11.2.2. Corrections based on CMB timing markers

The fitted time for each hit is corrected for the variation among the phases of the various clock domains and for the differences in fiber cable lengths. The correction for these effects is made with the FGD timing markers. A diagram of the FGD timing marker distribution is shown in Fig. 35.

The FGD Cosmic Trigger Module (CTM) has electrical LVDS connections to each of the 48 CMBs. When the MCM issues a trigger, the CTM sends a set of approximately simultaneous LVDS pulses to each CMB. Each CMB fans out these signals asynchronously and injects them into a spare channel on the FEB ASICs. Because

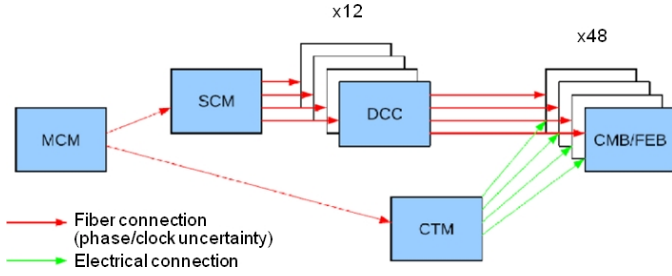


Figure 35: Diagram showing how the FGD timing marker pulses are distributed through the FGD-CTM. As can be seen, the timing marker generation is largely independent of the various optical fiber clock shifts associated with the FGD data readout chain.

the signals do not propagate through the digital  $\text{SCM} \rightarrow \text{DCC} \rightarrow \text{CMB}$  connections, they are not influenced by the various digital clock domains. The times of arrival of the timing markers at the FEBs are fixed relative to one another. Hence the differences in the times recorded for the timing marker pulses provide a measurement of the effects of these clock domain jitters and hence a way of correcting for the jitter. In practice the correction works as follows: for a particular hit, the difference between the timing marker for the ASIC of that hit relative to the timing marker for the first ASIC in the FGD is calculated; this difference is subtracted from the particular hit time.

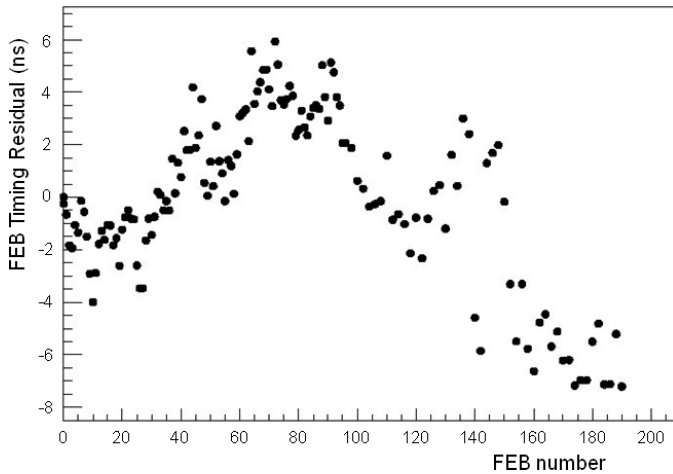


Figure 36: Measured FEB-to-FEB timing corrections.

### 11.2.3. FEB-to-FEB time corrections

A series of studies using cosmic rays has shown that while the timing markers account for clock jitters that vary from run to run and event to

event, there remain residual FEB-to-FEB time differences. These residual differences are not unexpected, since the CTM-CMB cable lengths are not identical, and the FGD CTM does not actually produce the timing markers at exactly the same time; the design of the CTM hardware and firmware makes this unavoidable.

However, the differences in the timing marker production times are found to be constant from event to event. We can therefore make an empirical correction for this residual difference using offsets calculated using cosmic tracks. For each track, the difference between the individual hit time and the track time averaged over all the hits is calculated. The residuals used in the correction are the average values of the difference calculated for a large number of cosmic rays. The set of measured corrections is shown in Fig. 36.

### 11.2.4. Calculation of final FGD time

The main utility of the FGD hit times is to calculate a time of passage through the FGD of a reconstructed track as an average time for the hits in the track. The hit times are first corrected for the light travel time down the WLS fiber, using the track information about the hit location. The dependence of this propagation time on hit location is calibrated by averaging over a large number of cosmic ray tracks while using the average track time as reference. The relationship between the measured time and the distance between the track crossing point along the bar and the MPPC is found to be not strictly linear. This phenomena is well reproduced by simulations accounting for the 17.2 cm/ns propagation speed, the photon reflections on the mirror and MPPC, and convoluting the photon arrival timing distribution with the electronics response function. The measured curve is used to correct for the effective propagation delay.

The single-hit timing resolution was measured by constructing histograms of the time difference between a given hit and a reference hit in the first FGD layer (with a correction for particle travel time) as a function of both the hit charge  $N_{av}$  and the reference hit charge. The widths of these curves for a particular reference hit charge are

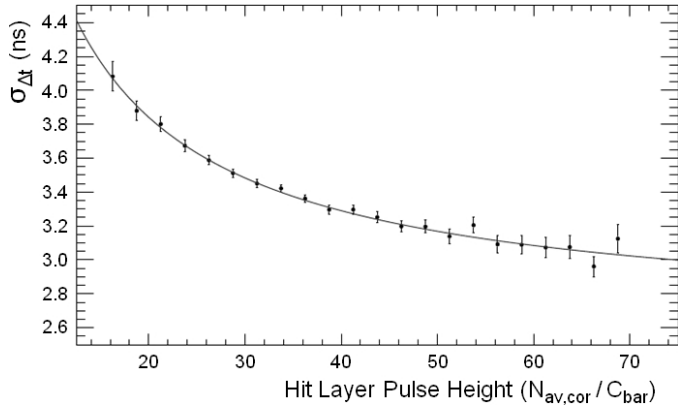


Figure 37: Spread of timing residuals  $\Delta t$  between the hit layer and reference layer as a function of the hit layer charge.

shown in Fig. 37 as a function of the “test” hit charge. They are well fitted by a constant contribution accounting for the average resolution for the reference hits added in quadrature with a contribution depending on the charge of the “test” hit:

$$\sigma_t(N_{av}) = \frac{12.5 \text{ ns}}{\sqrt{N_{av}}}. \quad (11)$$

Equation 11 could be interpreted as the single-hit time resolution if the statistical complications arising from, e.g., secondary avalanches and light reflection from the mirrored fiber ends could be neglected. The value of  $12.5 \pm 0.6$  ns might be interpreted as the single-avalanche timing resolution, which is closely related to the light decay time constants of scintillator and wavelength-shifting fiber, but smeared by light reflection from the mirrored fiber ends.

### 11.2.5. Tests of FGD timing resolution

A weighted average time for each FGD is calculated for reconstructed tracks, where the inverse weight is the expected timing resolution for a single hit associated with the track. The principal test of the FGD timing calibration is to look at the time difference between the two FGDs for FGD-triggered cosmic-ray events that hit both FGDs. In approximately half the events the muon hits FGD1 first; in the other half FGD2 is hit first. We use the fully calibrated time for each FGD track, calculated in the FGD reconstruction described in the previous sections.

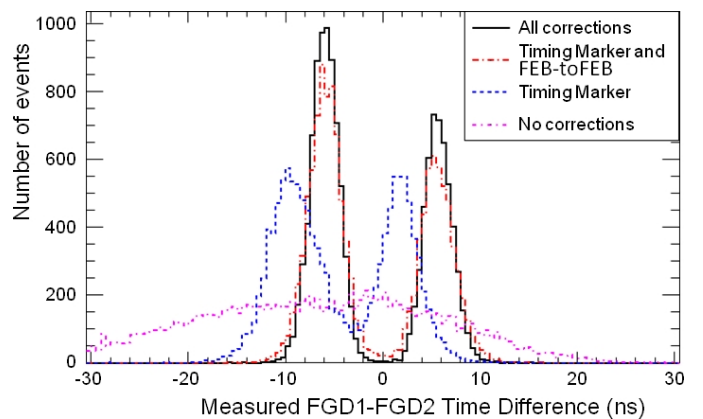
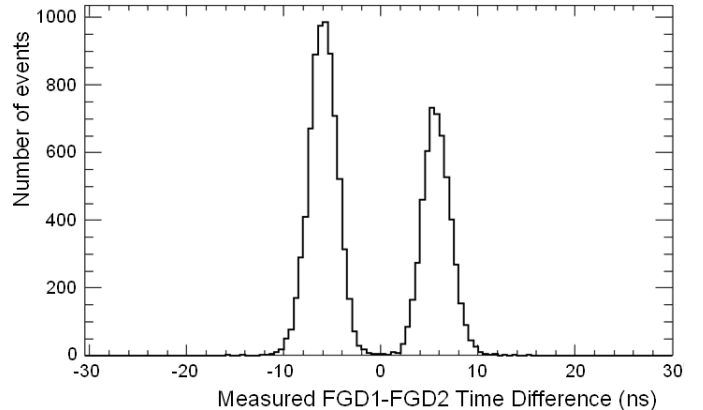


Figure 38: FGD1 - FGD2 time difference for FGD-triggered cosmic rays. The two peak structure is from cosmic rays that hit either FGD1 or FGD2 first. The upper plot shows the FGD1-FGD2 time differences with all corrections. The lower plot shows the FGD1-FGD2 time differences as the various corrections are applied.

The distribution of the difference between FGD1 and FGD2 track times is shown in the upper plot of Fig. 38. This plot shows the expected two peak structure, which comes from the fact that the cosmic muon hits either FGD1 or FGD2 first. The width of each FGD1-FGD2 peak for the fully corrected data curves is 1.47 ns. The clear separation of the two peaks shows that the FGD1-FGD2 time difference can be used to distinguish track directions between the two FGDs. The lower plot shows the effect of the various calibration stages. As expected, each calibration stage makes the distributions narrower.

## 12. M11 tests

Prior to shipment to Japan, assembled FGDs were installed in the M11 secondary beam line

at TRIUMF for testing. The goal of these tests was to calibrate and assess the performance of the FGD with beams of electrons, muons, pions and protons of known momenta. The tests were conducted during two running periods: in the fall of 2008 and spring of 2009. The earlier tests employed FGD1, with only a limited number of instrumented channels. Subsequently, one of the ND280 TPCs was installed upstream of the FGD. For later tests, FGD1 was fully instrumented. Finally, FGD1 was replaced by FGD2.

The location of the end of the M11 beamline is fixed. However, for the tests, the FGD was mounted on a rail system and could thus be moved horizontally to expose its entire width to the beam. It could also be rotated by up to  $45^\circ$ . Its vertical position could not be changed.

### 12.1. Beamline and M11 area

The TRIUMF cyclotron provides a 500 MeV proton beam composed of 3-4 ns wide bunches every 43 ns. Secondary particles are created via interactions of the primary beam in a beryllium production target (T1). The M11 channel views T1 at an angle of  $7^\circ$ . It consists of two bending magnets and six quadrupole magnets. Its length from T1 to the center of the final quadrupole is 13 m. The channel provides secondary charged particles:  $e$ 's,  $\mu$ 's, and  $\pi$ 's, of either polarity, with momenta up to 400 MeV/c. It also provides  $p$ 's up to 400 MeV/c, but these penetrate the FGD to a depth of only 6 cm.

For the FGD tests, a *front* plastic scintillator trigger counter was installed at the end of the beamline just downstream of the last magnet. A second, much larger, *back* plastic scintillator trigger counter was installed downstream of the FGD. Another possible trigger was provided by a movable plastic scintillator hodoscope located at an intermediate dispersed focus near the center of the channel.

At lower beam momentum, particle identification was based on time-of-flight through the channel using the relative times of the various trigger counters as well as the time provided by a capacitive pickup probe just upstream of the T1 production target. This method ceased to be useful

above  $\sim 250$  MeV/c because the times of flight become too similar to be distinguished. Nevertheless, it was possible to identify  $p$ 's by their large energy deposit in the front trigger counter. Below  $\sim 200$  MeV/c, demanding a coincidence between front and back trigger counters would select purely  $e$ 's, since heavier particles would range out in the FGD material.

The size of the beam spot at the FGD was  $\sim 15$  cm FWHM in the horizontal direction and  $\sim 8$  cm FWHM in the vertical. The angular spread of the beam was  $\sim 3^\circ$  FWHM. The beam flux varied with momentum and could be limited using sets of vertical and horizontal slits and jaws in the channel. Typical rates of  $\sim 10$  Hz were used for testing in order to match the capabilities of the developing data acquisition system.

### 12.2. Performance

Some measurements could be compared to Monte Carlo simulations, which were carried out using the same GEANT code as for the full ND280 detector [6], but with the addition of the M11 front trigger counter.

The simplest such comparison, not requiring calibration beyond a simple pulse height threshold, involved histogramming the number of hits in individual FGD layers for pions and muons of various incident momenta (electrons passed right through the FGD and protons stopped in the first few centimeters). The range can be varied through the thickness of the FGD by varying the incident momentum. One expects to see a uniform distribution of hits versus layer number in layers upstream of the layer corresponding to the particle's range at the given momentum, at which point most particles stop, so there is a sharp drop and few hits in layers downstream. The results of measurements at 190 MeV/c are shown in Fig. 39. Excellent agreement can be seen between data and Monte Carlo for this comparison. The distributions for pions are not as clean as for muons because of pion decays in flight upstream of the FGD. Qualitatively similar results were obtained for other momenta.

Having identified the FGD bar in which a muon has stopped, one can look for a second hit in the

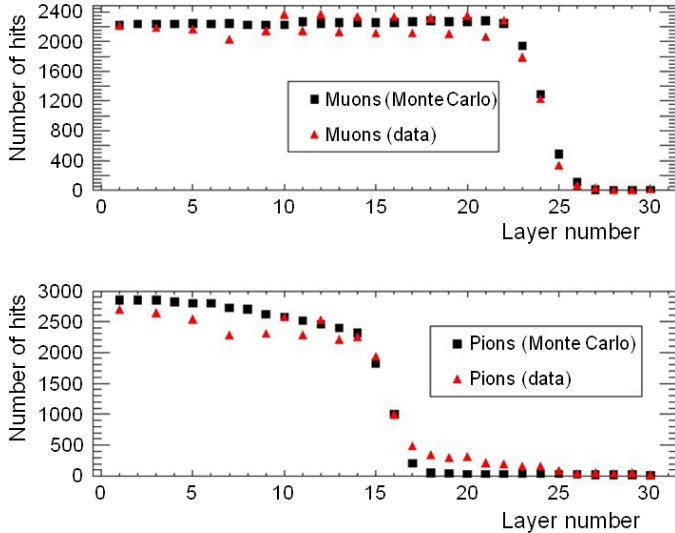


Figure 39: Comparison of data and Monte Carlo for the ranges of pions and muons in FGD1. The M11 channel was tuned to 190 MeV/c. Some channels were not instrumented at the time these measurements were made.

same bar at a later time, arising from muon decay. One expects the time distribution of such late hits to decrease exponentially, corresponding to the muon lifetime. Such measurements were made and found to be in agreement with expectations.

Electrons and positrons at M11 momenta are expected to pass through the FGD, depositing the same amount of energy in every layer. This feature proved useful in developing the FGD calibration chain described in detail in Section 11. Various effects that required correction were first identified in the M11 data analysis, and possible correction algorithms were tested and optimized using the  $e$  beam data. Temperature-dependent effects were particularly evident in the earliest runs since the cooling system described in Section 7.4 was not yet in place.

After calibration, several additional analyses and data/Monte Carlo comparisons could be performed:

- The most basic of these was a comparison of the pulse height distributions of  $e$ 's,  $\mu$ 's, and  $\pi$ 's in various FGD layers. Simulations agreed with the relative distributions observed and the data were used to adjust Monte Carlo parameters that had not yet

been optimized. For  $\mu$ 's and  $\pi$ 's stopping in the FGD,  $dE/dx$  increases as the particles slow down and the corresponding increase in pulse height was seen and matched by the simulations.

- The layer with the largest pulse height was taken to be a measure of muon range and the range was observed to vary with incident muon momentum in the way expected.
- Using an  $e$  beam, the hit information from vertical FGD bars was used to determine the hit location along the length of the horizontal bars. By translating the FGD horizontally, the dependence of pulse height on distance from the MPPC readout was measured to determine the light attenuation in the WLS fibers. The light attenuation curve measured in M11 agrees well with those determined from the fiber test-bed measurements described in Section 4, except at the very ends, where a deficit was observed in the test-beam results as described in Sec. 11.1.6. This feature was subsequently confirmed using cosmic rays *in situ* (see Section 13), as well as in bench tests.

### 12.3. MPPC saturation and Birks' effect

Figure 40 shows the observed FGD response (M) for  $\mu$ 's,  $\pi$ 's, and  $p$ 's, measured at various incident momenta in the first two layers of FGD1, normalized by the response measured for 350 MeV/c  $\pi$ 's, which we take as the value for minimum ionizing particles (mips). The results are plotted versus the similarly normalized calculated energy loss, also in units of mips. The left panel of the figure shows results corrected by a combination of elements of the calibration chain yielding  $N_{av,cor}/C_{bar}$  (see Eq. 6 in Sec. 11.1.3, and also Sec. 11.1.5). The middle panel shows the results with the MPPC saturation correction also applied, as described in Sec. 11.1.4, while the right panel shows the results with the Birks' correction described in Sec. 11.1.7 applied in addition. As can be seen, each correction improves the fit.



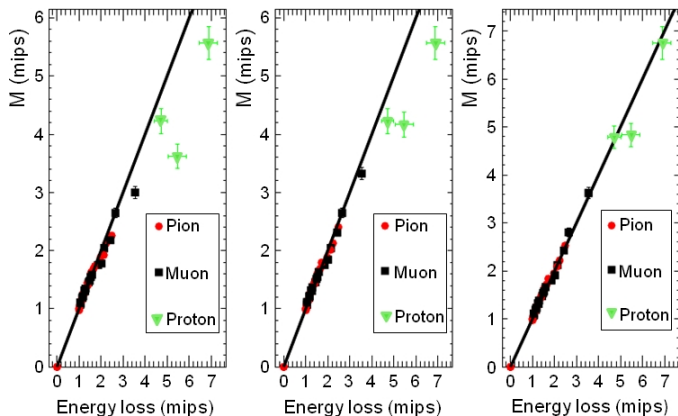


Figure 40: FGD responses for muons, pions and protons from various stages of the calibration chain, versus calculated energy loss. Both axes are normalized by the corresponding values for 350 MeV/c pions, which is taken to be the value for minimum ionizing particles. Left: calibration chain corrections applied; middle: saturation corrections also applied; right: correction for Birks' effect additionally applied. See text for details.

### 13. *In situ* Performance Measurements

The FGDs were shipped to the J-PARC laboratory in summer 2009, where they were inspected, re-assembled, and tested in the assembly building adjacent to the ND280 pit. In October 2009 both detectors were installed into the ND280 basket by overhead crane and services were connected. Commissioning and integration with the global DAQ continued through the remainder of 2009, and in February 2010 the ND280 detector as a whole began operations in the neutrino beam. The FGDs operated successfully during normal neutrino running (February - June 2010, December 2010 - March 2011), until operations were interrupted by the large March 11, 2011 earthquake in eastern Japan. Subsequent tests of the detectors with cosmic-ray triggers taken in the summer of 2011 showed no ill-effects resulting from the earthquake.

This section will highlight the operational performance of the detectors after installation into ND280.

#### 13.1. Reliability

The FGD hardware has operated reliably with minimal downtime since its installation. Regular studies of dark noise data and voltage scan

calibrations have been used to identify channels with abnormal signals. During the first period of T2K running (February - June 2010), approximately 30 FGD channels (out of 8448) appeared to be nonfunctional, typically showing an absence of dark noise pulses. These channels were scattered randomly across both detectors. In June 2010 one front-end board malfunctioned, turning off an additional 64 channels for the remainder of the month. This is the only example to date of a board-wide failure.

During the summer of 2010 the failed front-end board was replaced and an effort was mounted to reduce the number of isolated malfunctioning channels. It was found that about half the dead channels were caused by problems on the front-end board itself, most often a poor solder connection between the signal trace and the connector pin that plugs into the minirate backplane. By replacing or repairing such cards the number of dead channels was reduced to 17 (0.2 % of the detectors). These remaining channels are believed to be due to isolated faults on the backplanes themselves or else MPPC failures. Their number is low enough to represent a negligible problem for data-taking.

Because the MPPCs themselves are quite sensitive to temperature, the slow control system constantly monitors the environment inside the dark box. Fig. 41 shows the typical temperature variation over several days during normal beam running with the ND280 magnet closed and powered. The temperature variations are small enough that there is no need to adjust the operating voltages of the MPPCs to compensate, but instead these effects are compensated by the calibration chain (see Section 11).

#### 13.2. Hit efficiency

The hit efficiency of a scintillator bar may be estimated by analyzing cosmic-ray events that pass through an FGD. For simple cosmic-ray events with isolated tracks, hit efficiency may be estimated by looking at tracks that pass through several XY modules. If the track is reconstructed as passing through the  $n^{\text{th}}$  and  $n + 2^{\text{th}}$  layer, then a hit should have been recorded in layer  $n + 1$ .

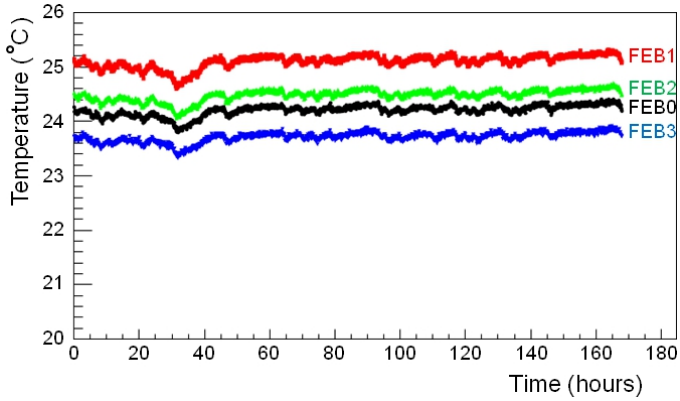


Figure 41: Temperature measured on four front-end boards inside the FGD1 dark box during neutrino running.

The fraction of the tracks where the middle layer is missing a hit gives the hit inefficiency.

Because the number of photoelectrons produced by a typical minimum ionizing particle ( $\sim 30$  pe) is much larger than the effective threshold of the pulse finder ( $\sim 0.5$  pe) or any analysis threshold ( $\sim 5$  pe), the hit inefficiency is dominated by tracks that pass through the inactive coating of the scintillator bar. This is illustrated in Fig. 42, which shows the hit efficiency for cosmic ray events as a function of angle or position across the bar. As a function of angle the inefficiency occurs primarily for tracks that move parallel to the coating of the bar itself. The size of the dip at zero angle corresponds approximately to the thickness of the coating divided by the bar width. In other words, the missed tracks are those that skim along the coating at the edge of a bar rather than passing through active scintillator. Viewed as a function of position on the bar, the efficiency is very high for tracks passing through the center of the bar, but drops off for tracks that hit the edges of the bar, which depending on their angle may again pass through the inactive coating and miss the active volume.

### 13.3. Light yield

The ND280 software is used to do a full Monte Carlo simulation of cosmic rays passing through the detector. The simulation includes a detailed GEANT4 model of the detectors. The processes of photon production and propagation in scintil-

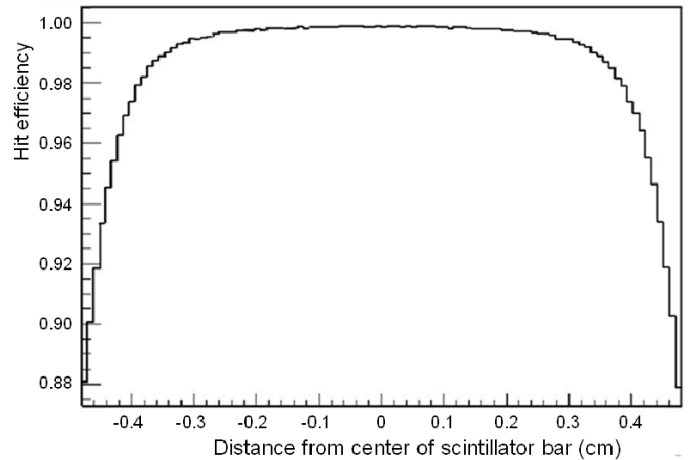
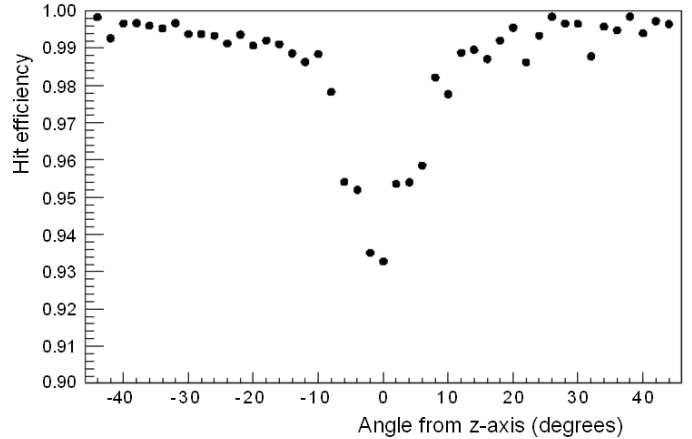


Figure 42: Measured hit efficiency as a function of track angle relative to bar axis (top) and position relative to bar width (bottom).

lator and fiber are not treated in a Monte Carlo technique, but rather using empirical analytic models for light attenuation in the fibers (as in the calibration chain) and the spatial distribution of the light incident on the MPPC pixel array that is derived from measurements with fibers [33]. Then the simulation returns to a Monte Carlo technique for the behavior of the MPPC. Optical photons are generated with this spatial distribution and with a time distribution given by the decay constants of light production in the scintillator and fiber together with the superposition of direct and reflected paths in the fiber. The MPPC behavior is simulated by a model that may generate a primary and possibly a secondary (possibly delayed) avalanche from each incident photon [28]. Each avalanche produces a charge impulse, the series of which is then processed by a model of the

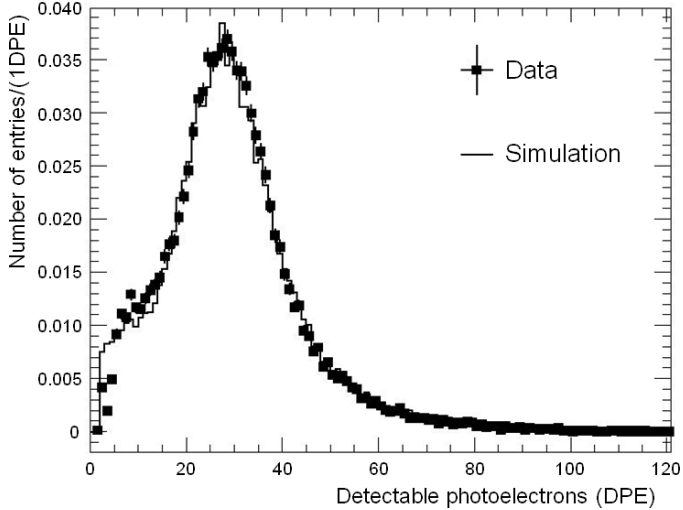


Figure 43: Measured spectrum of pulse heights processed to represent a quantity proportional to the number  $N_{scint}$  of scintillation photons (see Sec. 11.1.6), for cosmic ray events triggered by the FGDs. The data are compared to the corresponding result extracted from simulated events. The horizontal scale of the simulated spectrum is normalized to the data.

electronic analog and digital system. The simulation produces digitized MPPC waveforms, as well as logic signals from a model of the FGD’s self-trigger system.

Figure 43 shows the spectrum, for FGD-triggered cosmic ray events, of a measured quantity assumed to be proportional to the number of scintillation photons (see last paragraph of Sec. 11.1.6), superimposed upon a histogram of the same quantity extracted from reconstructed events from this simulation<sup>6</sup>.

The total number of photons detected in an MPPC should be proportional to the total deposited energy by a minimum ionizing particle in the active part of the scintillator bar, and hence to the path length of the track through the bar. Fig. 44 illustrates the measured MPPC avalanche yield from cosmic rays travelling through an FGD versus the calculated path length of the track through the bar. Although each bar is only 9.61 mm wide, much longer path lengths are possible for tracks with a direction component paral-

<sup>6</sup> The version of the simulation used for this figure employed a uniform distribution of photons incident on the MPPCs from the fibers.

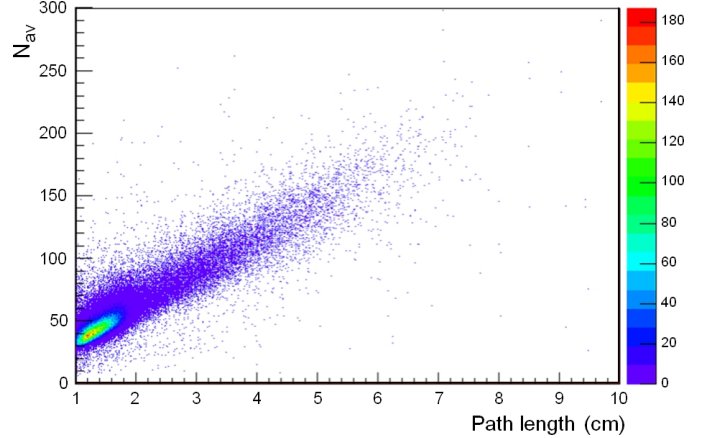


Figure 44: Correlation of the number  $N_{av}$  of MPPC avalanching pixels with path length through the scintillator bar.

lel to the bar’s axis.

#### 13.4. Particle identification

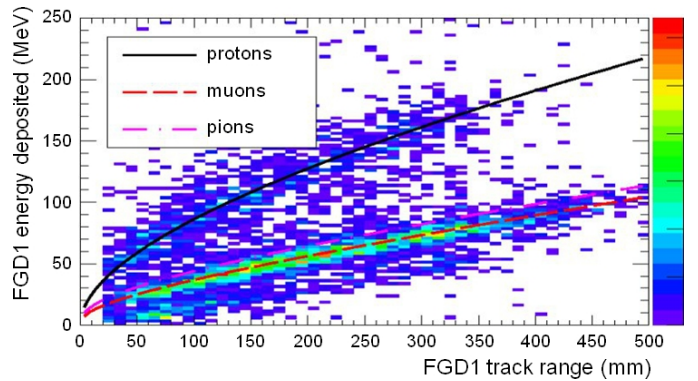


Figure 45: Deposited energy vs range for particles stopping in FGD1. The scatterplot shows stopping particles in neutrino beam data, while the curves show the MC expectations for protons, muons, and pions.

Because slower moving particles deposit more energy per path length, the energy loss summed over bars can be used to identify the type of particle that produced a track stopped in the FGD [17]. The measured light yield of a hit along a track is first converted into an equivalent energy deposit in MeV by the calibration chain described in Sec. 11, which includes corrections for MPPC gain and saturation, Birks’ constant effects, and the attenuation curve of the bar/fiber combination. By comparing the measured total energy deposit for a given particle range in the FGD to the theoretically expected energy deposit for

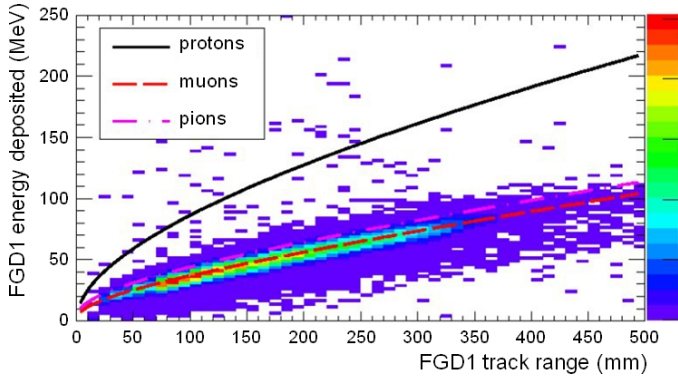


Figure 46: Deposited energy vs range for particles stopping in FGD1. The scatterplot shows stopping particles from cosmic ray triggers, while the curves show the MC expectations for protons, muons, and pions.

particles with that range, protons can be distinguished from muons and pions. Fig. 45 shows a scatterplot of deposited energy vs. range for particles produced by neutrino interactions and stopping in FGD1. The solid, dashed and dot-dashed lines show the expected locations of protons, muons, and pions, respectively, on this plot. A distinct population of protons can be discerned. In Fig. 46, similar distributions are shown for cosmic rays that stop in the FGD. In this case the muon line is well populated, as expected, but protons are of course absent.

### 13.5. Michel electron studies

Michel electrons produced by muons that stop in an FGD can be identified by looking for a delayed cluster of hits following the initial neutrino interaction. The FGD electronics reads out a  $10 \mu\text{s}$  waveform for each beam spill, while the beam bunches span an interval of just over  $4 \mu\text{s}$ . The electronics is therefore sensitive to Michel electrons for over four times the muon lifetime for muons produced early in the beam spill, dropping to about two and a half muon lifetimes for neutrino interactions late in the spill.

As a demonstration of the FGD’s ability to identify Michel electrons, we have looked for delayed clusters of hits following cosmic ray muon events. Stopping cosmic rays are selected by identifying muons that pass entirely through one FGD and enter the other FGD, without leaving hits in the far side of the second FGD. A “delayed clus-

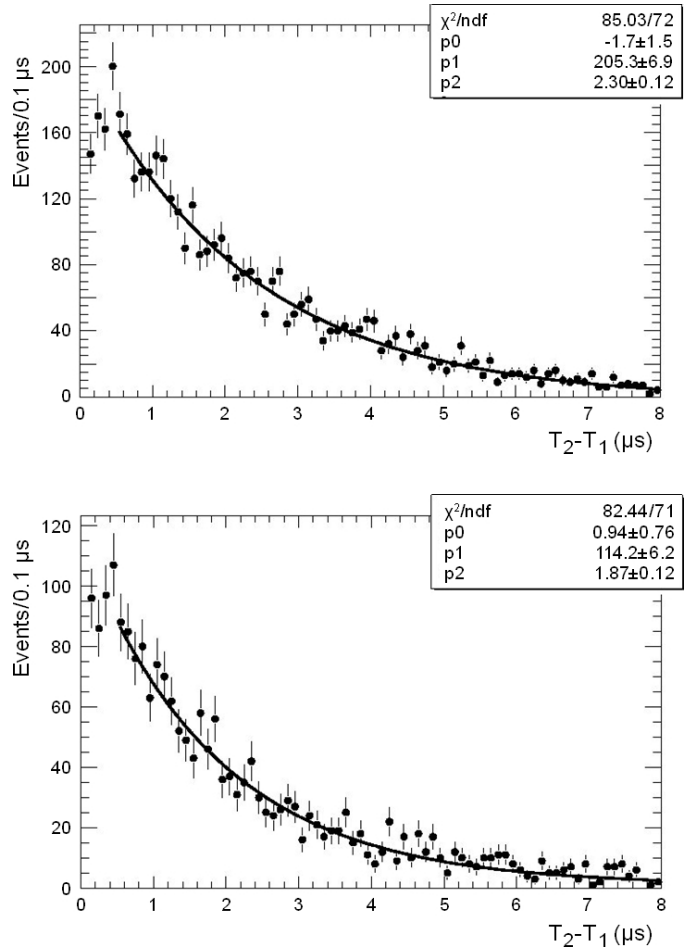


Figure 47: Measured lifetime distributions for positive muons (top) and negative muons (bottom) that stop inside an FGD. The data are fitted with an exponential plus a flat background. See text for details.

ter” is defined as a group of at least two hits that occurs at least  $100 \text{ ns}$  after any previous hits.

Fig. 47 shows the distribution of the time interval between the primary muon and the delayed cluster of hits for tracks stopping in the FGDs. The sign of the initiating muon can be determined from the track curvature in the magnetic field. Each fitted curve is the sum of an exponential decay with normalization  $p1$  and lifetime  $p2$  on top of a flat background  $p0$ . The fitted backgrounds are consistent with zero, as expected. For positive muons the fitted lifetime of  $2.23 \pm 0.09 \mu\text{s}$  is consistent with the muon lifetime, while for negative muons, the fitted lifetime ( $1.87 \pm 0.12 \mu\text{s}$ ) is shorter, since negative muons can become trapped in atomic states and then absorbed. The measured lifetime for negative muons is consistent

with previous measurements of the  $\mu^-$  capture lifetime on  $^{12}\text{C}$  [34].

### 13.6. Neutrino beam monitoring and stability

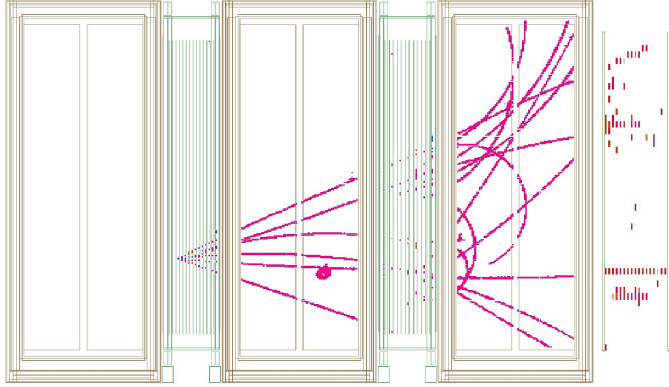


Figure 48: Sample ND280 event display for a neutrino interaction in the tracker. This appears to be a deep inelastic scattering interaction in FGD1.

Fig. 48 shows an event display of an actual neutrino event in the ND280 tracker. Most likely a neutrino has undergone deep inelastic scattering inside the first FGD, resulting in several particles that leave tracks in both FGDs and in the TPCs. The TPC track information is a key element of the FGD reconstruction and is used to associate hits to tracks for those particles that penetrate the TPCs.

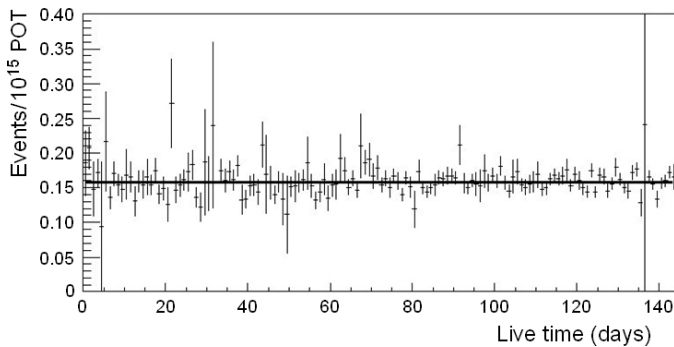


Figure 49: Measured neutrino interaction rate in the FGDs per POT as a function of day of beam running.

Using a set of low-level selection criteria, one can search for events that occur inside an FGD. Hits that occur in time with the expected neutrino beam bunch timing are selected and grouped in time if they occur within 10 ns of each other. Noise hits are rejected by a hit threshold of 2.5 pe

on individual hits and a requirement that there be at least two hits that total at least 10 photoelectrons. Finally, interactions that occurred in the FGD are selected by vetoing events with hits in the most upstream layers of the FGDs (to remove entering events from upstream), and at least 3 spatially contiguous hits are required in order to select track-like events. (These selection requirements are not the same as those used for T2K's normal analysis, but rather provide a low-level cross-check that uses only information from the FGDs but not other detectors.)

Fig. 49 shows the number of candidate interactions satisfying these criteria per proton delivered on target (POT), as a function of calendar time. The rate is constant, as expected. As the beam power gradually increased over the running period, one can see that the statistical uncertainties on each day's rate measurement generally decreased.

Fig. 50 shows the spatial distribution of hits in the  $x$  (horizontal) and  $y$  (vertical) coordinates of the FGD. Because T2K runs with an off-axis beam, we expected to see a decrease in the neutrino flux with increasing off-axis angle. This is observed, as the beam center is directed at  $X=+3.222$  m,  $Y=-8.146$  m, in the ND280 coordinate system.

Overall the results demonstrate that the FGDs are well-suited for measuring neutrino interactions from T2K's beam.

## 14. Acknowledgements

We would like to thank the support of the following agencies that made the T2K FGD project possible: Canada Foundation for Innovation, the Natural Sciences and Engineering Research Council (NSERC) of Canada, TRIUMF, and the National Research Council, Canada; MEXT and JSPS with Grant-in-Aid for Scientific Research on Priority Areas 18071007, Young Scientists S 20674004, JSPS Fellows, the Global COE Program The Next Generation of Physics, Spun from Universality and Emergence, Japan; and by the UK Science and Technology Facilities Council STFC, UK.

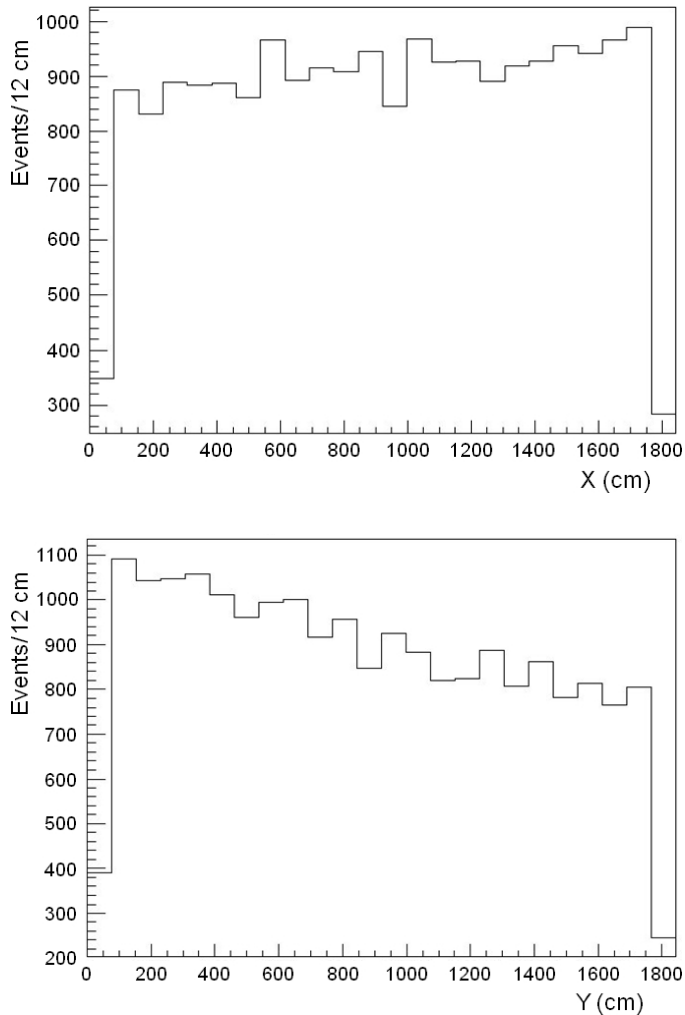


Figure 50: Vertex distribution in  $x$  (top) and  $y$  (bottom) inside the FGDs. The slopes indicate the change in flux with off-axis angle.

We would like to acknowledge D.Kolybaba, K.Wolbaum, C.Carbno, C.Ingram, B.Freitag, S.Schneider, B.Harack, A.Urichuk, A.Lim, T.Tolhurst and N.Hogan for their contributions to testing the WLS fibers, M. Goyette, W. Faszler, S. Sooriyakumaran, A. Starr and K. Hamano for their help with gluing the XY modules, and P. Lu for assistance with assembly, machining, and testing.

Thanks are owed to the entire T2K ND280 group for their support of this project. We would also like to thank the staff of the J-PARC center for their support and hospitality, the J-PARC Accelerator Group for providing the proton beam, and the T2K Beam Group for providing the neutrino beam. Support provided by KEK is also

gratefully acknowledged.

## References

- [1] Y. Itow, et al., The JHF-Kamioka neutrino project, [arXiv:hep-ex/0106019](https://arxiv.org/abs/hep-ex/0106019).
- [2] Y. Fukuda, T. Hayakawa, E. Ichihara, M. Ishitsuka, Y. Itow, et al., The Super-Kamiokande detector, *Nucl. Instrum. Meth.* A501 (2003) 418–462.
- [3] D. Beavis, A. Carroll, I. Chiang, et al., Long Baseline Neutrino Oscillation Experiment at the AGS (Proposal E889) Physics Design Report, BNL 52459 (1995).
- [4] A. K. Mann, Accelerator based, multiple detector long baseline neutrino oscillation experiment, Prepared for 3rd NESTOR Workshop, Pylos, Greece, 19-21 Oct., 1993.
- [5] R. L. Helmer, A New long baseline neutrino oscillation experiment at Brookhaven, Proc. 9th Lake Louise Winter Institute, Lake Louise, Canada, 1994, (World Scientific, 1995; eds. A. Astbury et al.), p. 291.
- [6] K. Abe, et al., The T2K Experiment (2011), accepted for publication in *Nucl. Instrum. Methods*, article in press, doi: 10.1016/j.nima.2011.06.067, [arXiv:1106.1238](https://arxiv.org/abs/1106.1238) [physics.ins-det].
- [7] N. Abgrall, P. Andrieu, B. and Baron, P. Bene, V. Berardi, et al., Time projection chambers for the T2K near detectors, *Nucl. Instrum. Meth.* A637 (2011) 25–46.
- [8] R. A. Smith, E. J. Moniz, Neutrino Reactions on Nuclear Targets, *Nucl. Phys.* B43 (1972) 605.
- [9] M. Ahn, et al., Measurement of Neutrino Oscillation by the K2K Experiment, *Phys. Rev.* D74 (2006) 072003.
- [10] V. Lyubushkin, et al., A Study of quasi-elastic muon neutrino and antineutrino scattering in the NOMAD experiment, *Eur. Phys. J.* C63 (2009) 355–381.
- [11] A. Aguilar-Arevalo, et al., First Measurement of the Muon Neutrino Charged Current Quasielastic Double Differential Cross Section, *Phys. Rev.* D81 (2010) 092005.
- [12] M. Yokoyama, et al., Development of multi-pixel photon counters, [arXiv:physics/0605241](https://arxiv.org/abs/physics/0605241).
- [13] S. Gomi, et al., Development and study of the multi pixel photon counter, *Nucl. Instrum. Meth.* A581 (2007) 427–432.
- [14] A. Pla-Dalmau, Extruded plastic scintillator for the MINOS calorimeters, *Frascati Phys. Ser.* 21 (2001) 513–522.
- [15] K. Nitta, E. Aliu, S. Andringa, S. Aoki, S. Choi, et al., The K2K SciBar detector, *Nucl. Instrum. Meth.* A535 (2004) 147–151.
- [16] B. C. Choudhary, Extruded Polystyrene Scintillator for MINOS, <http://minos-docdb.fnal.gov/0006/000676/001/numi0676.pdf>.

- [17] C. Licciardi, PhD thesis, University of Regina (2012), to be published.
- [18] Hamamatsu Photonics K. K., <http://www.hamamatsu.com>.
- [19] M. Yokoyama, et al., Performance of Multi-Pixel Photon Counters for the T2K near detectors, *Nucl. Instrum. Meth. A622* (2010) 567–573.
- [20] H. Kawamuko, T. Nakaya, K. Nitta, M. Yokoyama, Fiber connector for MPPC, *PoS PD07* (2006) 043.
- [21] D. Brook-Roberge, PhD thesis, University of British Columbia (2012), to be published.
- [22] S. Ritt, MSCB MIDAS Slow Control Bus, <https://midas.psi.ch/mscb>.
- [23] P. Baron, et al., AFTER, an ASIC for the readout of the large T2K time projection chambers, *IEEE Trans. Nucl. Sci.* 55 (2008) 1744–1752.
- [24] B. Kirby, PhD thesis, University of British Columbia (2012), to be published.
- [25] S. Ritt, P. Amaudruz, K. Olchanski, MIDAS (Maximum Integration Data Acquisition System) <http://midas.psi.ch>.
- [26] M. Thorpe, C. Angelsen, G. Barr, C. Metelko, T. Nicholls, G. Pearce, N. West, The T2K Near Detector Data Acquisition Systems, *IEEE Tran. Nucl. Sci.* 58 (2011) 1800–1806.
- [27] MPPC Specifications [http://sales.hamamatsu.com/assets/pdf/catsandguides/mppc\\_kapd0002e07.pdf](http://sales.hamamatsu.com/assets/pdf/catsandguides/mppc_kapd0002e07.pdf).
- [28] A. Vacheret, G. Barker, M. Dziewiecki, P. Guzowski, M. Haigh, et al., Characterization and Simulation of the Response of Multi Pixel Photon Counters to Low Light Levels, *Nucl.Instrum.Meth. A656* (2011) 69–83.
- [29] D. Orme, T. Nakaya, M. Yokoyama, A. Minamino, Measurement of PDE of MPPC with different wavelengths of light, *PoS International Workshop on New Photon Detectors* (2009) 019.
- [30] S. Hastings, The Saturation Calibration Of Tokai To Kamioka Fine Grained Scintillating Detector, PhD Thesis, University of British Columbia, Vancouver.
- [31] J. B. Birks, Theory and practice of scintillation counting, Macmillan, New York, 1964.
- [32] M. Hasegawa, Measurement of neutrino oscillation parameters with neutrino–nucleus interaction studies in the K2K experiment, PhD Thesis, Kyoto University.
- [33] M. Bryant, Plastic Scintillators for the T2K Fine-Grained Detector, MSc Thesis, University of British Columbia, Vancouver.
- [34] T. Suzuki, D. F. Measday, J. Roalsvig, Total Nuclear Capture Rates for Negative Muons, *Phys.Rev. C35* (1987) 2212.